Analysis and Optimization of Boost Converter Parameters in Internal Model Control for Voltage Source Converter-based AC Microgrids

Chiebuka Eyisi, *Student Member*, *IEEE*, and Qifeng Li, *Senior Member*, *IEEE*

***Abstract*—This paper investigates integration of distributed energy resources (DERs) in microgrids (MGs) through two-stage power conversion structures consisting of DC-DC boost converter and DC-AC voltage source converter (VSC) subsystems. In contrast to existing investigations that treated DC-link voltage as an ideal constant voltage, this paper considers the non-ideal dynamic coupling between both subsystems for completeness and higher accuracy, which introduces additional DC-side dynamics to the VSC. The analysis shows parameters of the boost converter's power model that impact stability through the DC-link. Carefully selecting these parameters can mitigate this effect on stability and improve dynamic performance across the DC-link. Hence, an optimization framework is developed to facilitate in selecting adequate boost converter parameters in designing a stable voltage source converter-based microgrid (VSC-MG). The developed optimization framework, based on particle swarm optimization, considers dynamic coupling between both subsystems and is also effective in avoiding inadequate boost converter parameters capable of propagating instability through the DC-link to the VSC. Simulations are performed with MATLAB/Simulink to validate theoretical analyses.**

***Index Terms*—AC microgrid, boost converter, dead-time, droop control, internal model control, particle swarm optimization, small-signal analysis, time delay, virtual impedance, voltage source converter.**

I. Introduction

DISTRIBUTED energy resources (DERs), including energy storage systems (ESSs) and distributed generation (DGs), are interfaced with power electronic converters, particularly DC-AC voltage source converters (VSCs), to enable interconnected microgrids (MGs) in either grid-connected or islanded modes of operation [1]. Converter-based MGs in low voltage distribution or medium voltage transmission networks, though beneficial in improving energy efficiency, power quality, reliability, and resiliency in the interconnected power network, suffer from low inertia which leads to challenges in preserving stability [2]. Control methods for VSCs are developed towards alleviating stability concerns and mitigating undesirable oscillations in interconnected MG networks [3]. Poportional-integral (PI) based control adopted to regulate bus voltages, network frequency, and injected currents is prominent and extensively used [4].

In a wide range of process control applications, the internal model control (IMC) has been used for disturbance rejection and tracking references in recent years with some applications towards VSC-interfaced DGs [5]. IMC was initially introduced in [6] with regards to chemical processes and emanates from the internal model principle stating that "control can be achieved if the control system encapsulates, either implicitly or explicitly, some representation of the process to be controlled" [7]. With a single tuning parameter, a trade-off can be provided between robustness to model inaccuracies and closed-loop performance [8]. IMC compares plant output with predicted output (acquired from a feed-forward path using an approximation of the plant). By utilizing a model of the plant in the IMC structure, model-based control is robust and provides a simple and systematic design procedure as an alternative to conventional control like PI-based control.

PI-based control, although easy to tune and effective, experiences a large overshoot, has a slow response, and a long settling time when compared to IMC method [5]. Small-signal models developed in [9] for IMC-based controllers followed a similar procedure in [10] and showed higher robustness to parameter changes, better eigenvalue (mode) patterns with regards to increased damping ratios and frequencies of sensitive eigenvalues, engendering better transient response and increased stability margins in comparison to PI-based controllers. These attributes translate to a better dynamic performance for IMC-based controllers compared to PI-based controllers as illustrated in [5], [9]. An improved transient response is valuable for VSC-interfaced DGs, so their operational limits are not violated allowing for better utilization. These reported methods investigating application of PI-based or IMC-based control in VSC-interfaced DGs neglected the impact of the DC-DC boost converter subsystem. DERs such as solar photovoltaic systems (PVs) or ESSs can be integrated in MGs through two-stage power conversion structures comprised of VSC and boost converter subsystems, where the boost converter increases low fluctuating voltage output of the resource to a regulated high DC-link voltage that

Manuscript received October 12, 2022; revised May 13, 2023, accepted June 20, 2023. Date of online publication September 8, 2023; date of current version August 26, 2024. This work is supported by the U.S. National Science Foundation under Grant #2124849.

C. Eyisi (ORCID: https://orcid.org/0000-0002-7728-9776) and Q. Li (corresponding author, email: qifeng.li@ucf.edu; ORCID: https://orcid.org/0000-0001-9754-0801) are with the Department of Electrical and Computer Engineering, University of Central Florida, Orlando, FL 32816 USA.

DOI: 10.17775/CSEEJPES.2022.06880

is fed to the VSC [11]. Analyzing control of voltage source converter-based microgrids (VSC-MGs) should therefore incorporate both subsystems for completeness.

Recent investigations in control of VSC-interfaced DGs consider more detailed models that incorporate the effects of the digital controller's time delay in state-space modeling via a *Padé* approximation [12]. Additionally, effects of dead-time and computational time delays produced during switching processes were incorporated into the VSC's small-signal model in [13]. It was observed that some low-to-medium frequency modes were highly sensitive to states associated with modeling these effects and should not be ignored, especially when using inductor-capacitor-inductor (LCL) filters. By incorporating IMC-based controllers in a VSC, this paper examines DC-link voltage regulation through a boost converter with applicable PI-based control framework. Effects related to time delay of an implemented digital control algorithm, and dead-time effect associated with VSCs in an islanded MG network are also considered. Detailed modeling is achieved by adopting the graphical modeling approach in [14].

Instability can originate through an unstable mode from either the DC or AC terminal of the VSC subsystem, and in some cases, stability at both terminals is not equivalent [15]. Consideration of the DC-link voltage terminal as an ideal constant voltage source introduces no additional DC-side dynamics to the VSC [9], [10], [12], and therefore results in an incomplete analysis for DGs with boost converter subsystems. For higher accuracy, the impact of non-ideal DC-link voltage terminal between both subsystems is necessary in analyzing stability and cannot be neglected. The work in [16] investigated interaction between both subsystems; however, did not account for the effect of the VSC's dead-time via the LCL filter and the VSC's power controller that governs power sharing within the network. Instability due to an unstable mode from the DC-side presents the need for its inclusion in stability analysis and the need to optimize parameters in the boost converter subsystem that impact stability. Existing literature investigating optimization of boost converter parameters focuses on aspects of weight, volume, voltage and current ripples, efficiency, and cost [17]–[19], but no consideration was made towards its non-ideal interaction with an interfacing VSC in regard to small-signal stability. The findings of this paper include:

1) Consideration of DC-link voltage as an ideal constant voltage result in an incomplete analysis for DGs with boost converter subsystems. Instability propagates through the DC-link due to unstable mode(s) highly influenced by parameters of the boost converter. Careful selection of these parameters improves dynamic performance across the DC-link.

2) An optimization framework to aid in selecting these parameters is developed to mitigate this effect on stability from the boost converter subsystem. To ensure trade-off between steady-state and dynamic performance while designing a stable VSC-MG, the optimization framework incorporates particle swarm optimization (PSO) to obtain adequate boost converter parameters and avoids inadequate boost converter parameters capable of propagating instability from the boost converter subsystem to the VSC subsystem.

The optimization framework developed in this paper considers dynamic coupling between the boost converter and VSC subsystems while addressing aspects of small-signal stability. The remainder of the paper is organized as follows. Small-signal state-space models for components in the boost converter and VSC subsystems including the associated line and load dynamics for a VSC-MG are described in Section II. Section III presents eigenvalue and participation factor analyses on an islanded test VSC-MG network combining both subsystems. Dominant modes in the network reveal critical parameters in the boost converter subsystem that impact stability in the DC-link. Further investigation under different operating conditions reveals these same modes remain dominant. An optimization framework utilizing PSO is developed in Section IV. The resulting dynamic performance demonstrates the need for careful selection of boost converter parameters by combining both subsystems for small-signal stability assessment. Section V concludes the paper.

II. VSC-MG Small-signal State-space Modeling

MG networks operating in either grid-connected or islanded modes require network frequency and bus voltages to be maintained at appropriate levels. In grid-connected operating mode, this responsibility is on the utility grid, whereas in islanded operating mode, the DERs maintain both quantities in the MG network. An objective for control methods adopted in VSC-interfaced DGs is to aid in preserving stability and improve transient response of bus voltages, network frequency, and injected currents in VSC-MGs. Small-signal stability is investigated in these MG networks by performing eigenvalue, sensitivity, and participation factor analyses; and then the control method adopted is validated through experimental setups or computer simulations of the modeled components in the MG network.

The investigated MG in this paper consists of DERs such as PVs or ESSs that are integrated through two-stage power conversion structures comprised of DC-DC boost converter and DC-AC VSC subsystems. Analysis presented in the paper can be applied to VSC-MG networks that integrate other types of DERs through similar structures. For DERs with a relatively low fluctuating output voltage, a boost converter would be required to raise low voltage to a regulated high DC-link voltage suitable for VSC's connection to meet voltage requirements of the interconnected network. Small-signal state-space models are illustrated for each component in the VSC-MG for both boost converter and VSC subsystems via equations as a set of input, output, and state variables describing system dynamics. State-space models are represented by linearizing these equations around stable operating points. By integrating small-signal state-space models for both subsystems, interaction between both subsystems considering non-ideal DC-link voltage terminal can be investigated using eigenvalue, sensitivity, and participation factor analyses.

A. Boost Converter Subsystem

The complete block diagram of the boost converter subsystem showing interconnection between the boost converter, the

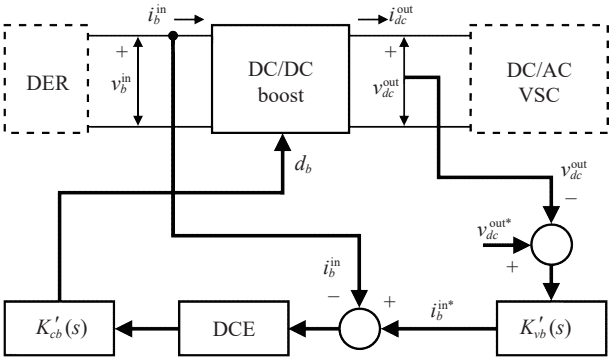

Fig. 1. Boost converter subsystem.

inner current controller, the digital control emulator (DCE) model block, and the outer voltage controller is shown in the Fig. 1.

1) Voltage Controller

PI-based outer voltage controller providing the reference to the boost converter's current controller can be found in [14] and is shown:

$$[\Delta\dot{\phi}_b] = \underbrace{[0]}_{A_{Vb}}[\Delta\phi_b] + \underbrace{[1]}_{B1_{Vb}}[\Delta v_{dc}^{\text{out}*}] + \underbrace{[-1]}_{B2_{Vb}}[\Delta v_{dc}^{\text{out}}] \tag{1}$$

$$[\Delta i_b^{\text{in}*}] = \underbrace{[K'_{ivb}]}_{C_{Vb}}[\Delta\phi_b] + \underbrace{[K'_{pvb}]}_{D1_{Vb}}[\Delta v_{dc}^{\text{out}*}] + \underbrace{[-K'_{pvb}]}_{D2_{Vb}}[\Delta v_{dc}^{\text{out}}] \tag{2}$$

where $\dot{\phi}_b$ is the error between the reference DC-link output voltage $v_{dc}^{\text{out}*}$ and the measured DC-link output voltage v_{dc}^{out}, whereas the boost converter's input current reference is $i_b^{\text{in}*}$. The voltage controller of the boost converter subsystem compares v_{dc}^{out} with $v_{dc}^{\text{out}*}$ and generates $i_b^{\text{in}*}$. The proportional and integral coefficients of the voltage controller are K'_{pvb} and K'_{ivb} respectively, both represented with transfer function $K'_{vb}(s) = (K'_{pvb} + K'_{ivb}/s)$ in Fig. 1.

2) Current Controller

PI-based inner current controller providing the boost converter's duty cycle can be found in [14] and is shown:

$$[\Delta\dot{\gamma}_b] = \underbrace{[0]}_{A_{Cb}}[\Delta\gamma_b] + \underbrace{[1]}_{B1_{Cb}}[\Delta i_b^{\text{in}*}] + \underbrace{[-1]}_{B2_{Cb}}[\Delta i_b^{\text{in}}] \tag{3}$$

$$[\Delta d_b] = \underbrace{[K'_{icb}]}_{C_{Cb}}[\Delta\gamma_b] + \underbrace{[K'_{pcb}]}_{D1_{Cb}}[\Delta i_b^{\text{in}*}] + \underbrace{[-K'_{pcb}]}_{D2_{Cb}}[\Delta i_b^{\text{in}}] \tag{4}$$

where $\dot{\gamma}_b$ is the error between the reference input current $i_b^{\text{in}*}$ and the measured input current i_b^{in}, whereas the boost converter's duty cycle is d_b. The current controller of the boost converter subsystem compares i_b^{in} with $i_b^{\text{in}*}$ and generates d_b. Proportional and integral coefficients of the current controller are K'_{pcb} and K'_{icb} respectively, both represented with transfer function $K'_{cb}(s) = (K'_{pcb} + K'_{icb}/s)$ in Fig. 1.

3) Power Model

The complete derivation of the boost converter power model in Fig. 2, including its state-space model showing combinations of turn-on and turn-off states can be found in [14], [16] and is as shown:

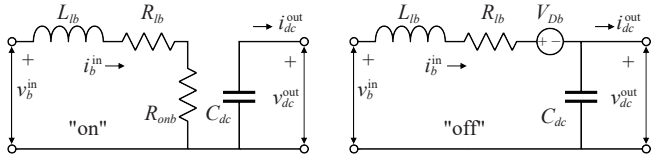

Fig. 2. Boost converter power model.

$$\begin{bmatrix}\Delta\dot{i}_b^{\text{in}} \\ \Delta\dot{v}_{dc}^{\text{out}}\end{bmatrix} = \underbrace{\begin{bmatrix}\frac{-R_{lb}-D_bR_{onb}}{L_{lb}} & \frac{-1+D_b}{L_{lb}} \\ \frac{1-D_b}{C_{dc}} & 0\end{bmatrix}}_{A_{Pb}}\begin{bmatrix}\Delta i_b^{\text{in}} \\ \Delta v_{dc}^{\text{out}}\end{bmatrix} + \underbrace{\begin{bmatrix}\frac{1}{L_{lb}} \\ 0\end{bmatrix}}_{B1_{Pb}}[\Delta v_b^{\text{in}}] + \underbrace{\begin{bmatrix}\frac{V_{dc}^{\text{out}}+V_{Db}-R_{onb}I_b^{\text{in}}}{L_{lb}} \\ -\frac{I_b^{\text{in}}}{C_{dc}}\end{bmatrix}}_{B2_{Pb}}[\Delta d_b] + \underbrace{\begin{bmatrix}0 \\ -\frac{1}{C_{dc}}\end{bmatrix}}_{B3_{Pb}}[\Delta i_{dc}^{\text{out}}] \tag{5}$$

$$\begin{bmatrix}\Delta i_b^{\text{in}} \\ \Delta v_{dc}^{\text{out}}\end{bmatrix} = \underbrace{\begin{bmatrix}1 & 0 \\ 0 & 1\end{bmatrix}}_{C_{Pb}}\begin{bmatrix}\Delta i_b^{\text{in}} \\ \Delta v_{dc}^{\text{out}}\end{bmatrix} + \underbrace{\begin{bmatrix}0 & 0 & 0 \\ 0 & 0 & 0\end{bmatrix}}_{D_{Pb}}\begin{bmatrix}\Delta v_b^{\text{in}} \\ \Delta d_b\end{bmatrix} \tag{6}$$

where R_{lb}, L_{lb}, C_{dc}, and R_{onb} are the internal resistance and inductance of the input filter inductor, the capacitance of the output DC-link capacitor, and the resistance of the switching device in its "on-state" respectively. The diode's forward voltage drop and the boost converter's duty cycle are V_{Db} and d_b respectively. The input and output voltages are v_b^{in} and v_{dc}^{out}, whereas the input and output currents are i_b^{in} and i_{dc}^{out}. The power model captures an average switching cycle (turn-on and turn-off states) of the boost converter subsystem using i_b^{in}, i_{dc}^{out}, v_b^{in}, and v_{dc}^{out}. The steady-state values of the output voltage, the input current, and the duty cycle of the boost converter are V_{dc}^{out}, I_b^{in}, and D_b respectively.

4) Digital Control Emulator (DCE) for Boost

In [20], DCE is a continuous transfer function expression describing the combination of digital implementation of the control algorithm as a transport delay, an ideal sampler, and a zero-order hold (ZOH) and is as shown:

$$G_{\text{DCE}}(s) = \mathrm{e}^{-sT_s}\frac{1}{T_s}\frac{1-\mathrm{e}^{-sT_s}}{s} \tag{7}$$

where T_s refers to sampling period delay. Computational or time delays introduce complications in execution because they make transfer functions irrational. The *Padé* approximation can be applied to (7) and is one of the common approximations by poles and zeros for delays used to obtain rational transfer functions. This leads to finite states being added to the state-space model and aid in revealing interactions among states and effects of computational and time delays. The equivalent linear state-space model generated follows the *Padé* approximation as demonstrated in [21] and is applied to all input signals ($i_b^{\text{in}*}$ and i_b^{in}) to boost converter's current controller.

B. VSC Subsystem

A complete block diagram of the VSC subsystem showing interconnection between the VSC, the LCL filter and dead-time model block, the power controller, the virtual impedance

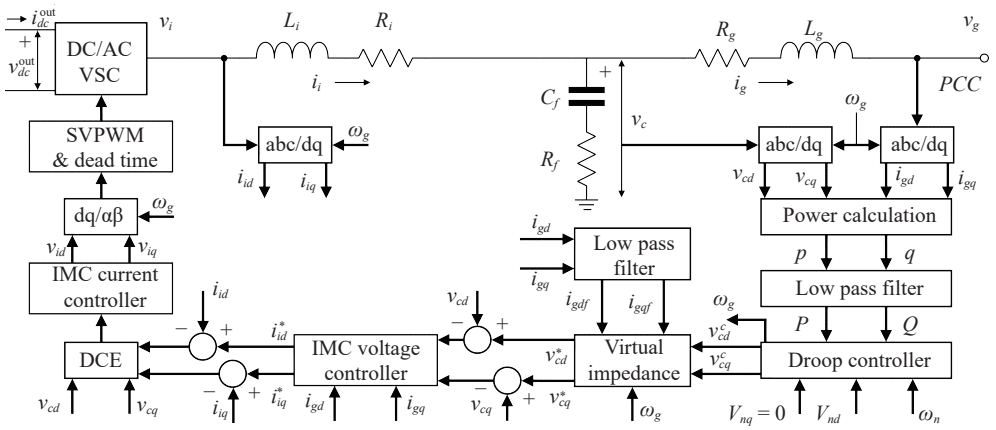

Fig. 3. VSC subsystem.

model block, the DCE model block, and the inner current controller and outer voltage controller is shown in the Fig. 3.

1) Voltage Controller

The IMC-based outer voltage controller is shown in Fig. 4 with more detailed information available in [5], and the corresponding state-space model found in [9] is as shown:

$$\begin{bmatrix}\Delta\dot{\phi}_d\\ \Delta\dot{\phi}_q\end{bmatrix} = \underbrace{\begin{bmatrix}0 & 0\\ 0 & 0\end{bmatrix}}_{A_{Vvsc}}\begin{bmatrix}\Delta\phi_d\\ \Delta\phi_q\end{bmatrix} + \underbrace{\begin{bmatrix}1 & 0\\ 0 & 1\end{bmatrix}}_{B1_{Vvsc}}\begin{bmatrix}\Delta v^*_{cd}\\ \Delta v^*_{cq}\end{bmatrix} + \underbrace{\begin{bmatrix}-1 & 0\\ 0 & -1\end{bmatrix}}_{B2_{Vvsc}}\begin{bmatrix}\Delta v_{cd}\\ \Delta v_{cq}\end{bmatrix} \tag{8}$$

$$\begin{bmatrix}\Delta i^*_{id}\\ \Delta i^*_{iq}\end{bmatrix} = \underbrace{\begin{bmatrix}0 & -K'_{iv}\\ K'_{iv} & 0\end{bmatrix}}_{C_{Vvsc}}\begin{bmatrix}\Delta\phi_d\\ \Delta\phi_q\end{bmatrix} + \underbrace{\begin{bmatrix}K_{pv} & -K'_{pv}\\ K'_{pv} & K_{pv}\end{bmatrix}}_{D1_{Vvsc}}\begin{bmatrix}\Delta v^*_{cd}\\ \Delta v^*_{cq}\end{bmatrix} + \underbrace{\begin{bmatrix}-K_{pv} & K'_{pv}\\ -K'_{pv} & -K_{pv}\end{bmatrix}}_{D2_{Vvsc}}\begin{bmatrix}\Delta v_{cd}\\ \Delta v_{cq}\end{bmatrix} + \underbrace{\begin{bmatrix}F_C & 0\\ 0 & F_C\end{bmatrix}}_{D3_{Vvsc}}\begin{bmatrix}\Delta i_{gd}\\ \Delta i_{gq}\end{bmatrix} \tag{9}$$

where $\dot{\phi}_{dq}$ is the error between the reference output capacitor voltage v^*_{cdq} and the measured output capacitor voltage v_{cdq} in d-q reference frame. IMC-based outer voltage controller constitutes proportional-derivative (PD) and PI controllers represented by transfer functions $K_v(s) = (K_{pv} + sK_{dv})$ and $K'_v(s) = (K'_{pv} + K'_{iv}/s)$ respectively, with tuning coefficients $K_{pv} = C_f/\lambda_v$, $K_{dv} = C_f T_c/\lambda_v$, $K'_{pv} = \omega_n C_f T_c/\lambda_v$, and $K'_{iv} = \omega_n C_f/\lambda_v$, in which ω_n is a nominal frequency operating point, C_f models filter capacitance of the LCL filter, λ_v is the closed-loop time constant of the voltage control loop, and T_c is time constant of the equivalent model of the current control loop [5]. Derivative coefficient K_{dv} is reasonably ignored in the state-space model to yield adequate transfer functions due to its value being 200 times smaller than K_{pv} in this study. d-q components of VSC output current reference and injected grid current are i^*_{idq} and i_{gdq} respectively. The voltage control loop of the VSC subsystem compares v_{cdq} with v^*_{cdq} and generates i^*_{idq}. F_C is the feed-forward control gain of the injected grid current i_{gdq} into the voltage control loop.

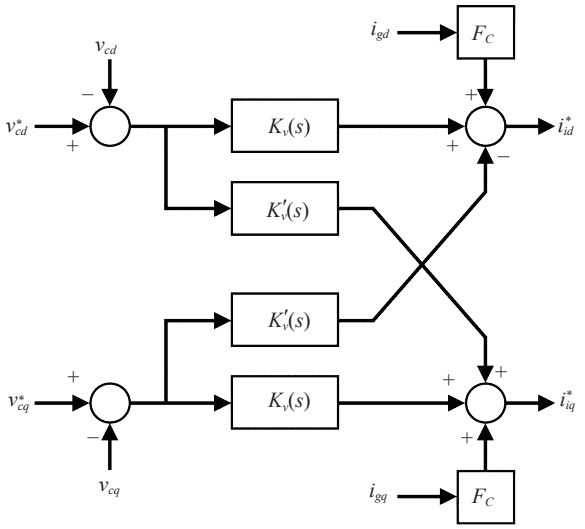

Fig. 4. IMC-based voltage controller.

2) Current Controller

IMC-based inner current controller is shown in Fig. 5 with more detailed information available in [5], and the corresponding state-space model found in [9] is shown:

$$\begin{bmatrix}\Delta\dot{\gamma}_d\\ \Delta\dot{\gamma}_q\end{bmatrix} = \underbrace{\begin{bmatrix}0 & 0\\ 0 & 0\end{bmatrix}}_{A_{Cvsc}}\begin{bmatrix}\Delta\gamma_d\\ \Delta\gamma_q\end{bmatrix} + \underbrace{\begin{bmatrix}1 & 0\\ 0 & 1\end{bmatrix}}_{B1_{Cvsc}}\begin{bmatrix}\Delta i^*_{id}\\ \Delta i^*_{iq}\end{bmatrix} + \underbrace{\begin{bmatrix}-1 & 0\\ 0 & -1\end{bmatrix}}_{B2_{Cvsc}}\begin{bmatrix}\Delta i_{id}\\ \Delta i_{iq}\end{bmatrix} \tag{10}$$

$$\begin{bmatrix}\Delta v_{id}\\ \Delta v_{iq}\end{bmatrix} = \underbrace{\begin{bmatrix}K_{ic} & -K'_{ic}\\ K'_{ic} & K_{ic}\end{bmatrix}}_{C_{Cvsc}}\begin{bmatrix}\Delta\gamma_d\\ \Delta\gamma_q\end{bmatrix} + \underbrace{\begin{bmatrix}K_{pc} & -K'_{pc}\\ K'_{pc} & K_{pc}\end{bmatrix}}_{D1_{Cvsc}}\begin{bmatrix}\Delta i^*_{id}\\ \Delta i^*_{iq}\end{bmatrix} + \underbrace{\begin{bmatrix}-K_{pc} & K'_{pc}\\ -K'_{pc} & -K_{pc}\end{bmatrix}}_{D2_{Cvsc}}\begin{bmatrix}\Delta i_{id}\\ \Delta i_{iq}\end{bmatrix} + \underbrace{\begin{bmatrix}F_V & 0\\ 0 & F_V\end{bmatrix}}_{D3_{Cvsc}}\begin{bmatrix}\Delta v_{cd}\\ \Delta v_{cq}\end{bmatrix} \tag{11}$$

where $\dot{\gamma}_{dq}$ is the error between the reference VSC output current i^*_{idq} and the measured VSC output current i_{idq} in d-q reference frame. IMC-based inner current controller consti-

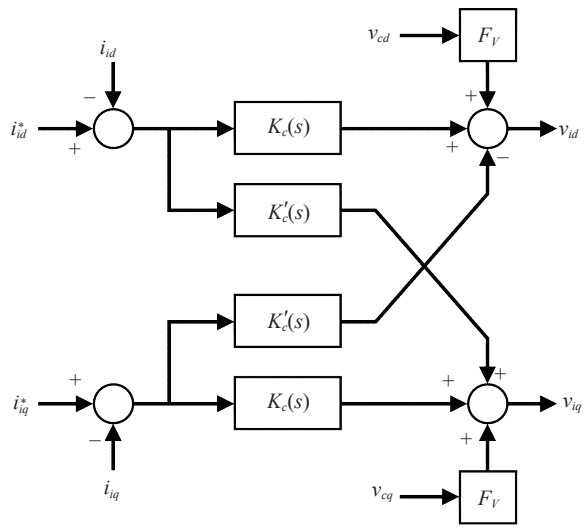

Fig. 5. IMC-based current controller.

tutes proportional-integral-derivative (PID) and PI controllers represented by transfer functions $K_c(s) = (K_{pc} + K_{ic}/s + sK_{dc})$ and $K'_c(s) = (K'_{pc} + K'_{ic}/s)$ respectively, with tuning coefficients $K_{pc} = (R_i T_{pwm} + L_i)/\lambda_c$, $K_{ic} = (R_i - T_{pwm}\omega_n^2 L_i)/\lambda_c$, $K_{dc} = T_{pwm}L_i/\lambda_c$, $K'_{pc} = 2T_{pwm}\omega_n L_i/\lambda_c$, and $K'_{ic} = \omega_n(R_i T_{pwm} + L_i)/\lambda_c$, in which L_i and R_i model VSC-side inductance of the LCL filter, λ_c is the closed-loop time constant of current control loop, and T_{pwm} models VSC as a time delay [5]. Similarly, derivative coefficient K_{dc} is reasonably ignored in the state-space model to yield adequate transfer functions due to its value being a few orders of magnitude smaller than K_{pc} and K_{ic} in this study. d-q components of VSC output voltage and output capacitor voltage are v_{idq} and v_{cdq} respectively. The current control loop of the VSC subsystem compares i_{idq} with i^*_{idq} and generates v_{idq}. F_V is the feed-forward control gain of output capacitor voltage v_{cdq} into current control loop.

3) Power Controller

The power controller governs sharing of active (P) and reactive (Q) power between VSCs in steady-state and is comprised of a power calculation block, a low-pass filter, and a droop controller. As seen in Fig. 3, the power calculation block yields instantaneous active (p) and reactive (q) power. Additionally, other inputs to the droop controller include the nominal frequency operating point ω_n, and the nominal voltage operating point V_{ndq} in the d-q reference frame. Equivalent derivations of the droop control-based power controller including its state-space model can be found in [9], [10], [14] and is as shown:

$$\begin{bmatrix}\Delta\dot{\delta}\\ \Delta\dot{P}\\ \Delta\dot{Q}\end{bmatrix} = \underbrace{\begin{bmatrix}0 & -m_p & 0\\ 0 & -\omega_{cpc} & 0\\ 0 & 0 & -\omega_{cpc}\end{bmatrix}}_{A_{Pvsc}}\begin{bmatrix}\Delta\delta\\ \Delta P\\ \Delta Q\end{bmatrix} + \underbrace{\begin{bmatrix}-1\\ 0\\ 0\end{bmatrix}}_{B2_{Pvsc}}\begin{bmatrix}\Delta\omega_{gcom}\end{bmatrix} + \frac{3}{2}\omega_{cpc}\underbrace{\begin{bmatrix}0 & 0 & 0 & 0\\ I_{gd} & I_{gq} & V_{cd} & V_{cq}\\ -I_{gq} & I_{gd} & V_{cq} & -V_{cd}\end{bmatrix}}_{B1_{Pvsc}}\begin{bmatrix}\Delta v_{cd}\\ \Delta v_{cq}\\ \Delta i_{gd}\\ \Delta i_{gq}\end{bmatrix} \quad (12)$$

$$\begin{bmatrix}\Delta\omega_g\\ \Delta v^c_{cd}\\ \Delta v^c_{cq}\end{bmatrix} = \underbrace{\begin{bmatrix}0 & -m_p & 0\\ 0 & 0 & -n_q\\ 0 & 0 & 0\end{bmatrix}}_{C_{Pvsc}}\begin{bmatrix}\Delta\delta\\ \Delta P\\ \Delta Q\end{bmatrix} \quad (13)$$

where δ is phase angle difference between an individual VSC's reference frame and a common reference frame rotating at ω_{gcom}. The reference frame of one of the VSCs can be chosen as the common reference frame. The low-pass filtered active and reactive power, P and Q are average values to be used in a droop controller that provides a degree of negative feedback similar to conventional synchronous machines. The cut-off frequency of the low-pass filter in the power controller is ω_{cpc}. The active and reactive power droop gains are m_p (in rad/s/W) and n_q (in V/Var) respectively. d-q components of the output capacitor voltage and injected grid current are v_{cdq} and i_{gdq}, with corresponding steady-state values V_{cdq} and I_{gdq} respectively. The droop-governed frequency of the VSC when it's providing active power P is ω_g and d-q components of the droop-governed command output capacitor voltage when VSC is providing reactive power Q is v^c_{cdq}.

4) LCL Filter with Dead-time Effect

The addition of dead-time effect in the VSC subsystem was shown to introduce a damping effect as presented in [22]. For an LCL filter, the nonlinear function expressed in (14) is incorporated to model the dead-time effect with continuous space vector pulse width modulation (SVPWM) [13].

$$f_d(i_{idq}) = -\frac{1}{L_i}\frac{T_d}{T_{sw}}\frac{2\sqrt{6}}{\pi}\begin{bmatrix}\frac{i_{id}}{\sqrt{i_{id}^2+i_{iq}^2}}v_{dc}^{\text{out}}\\ \frac{i_{iq}}{\sqrt{i_{id}^2+i_{iq}^2}}v_{dc}^{\text{out}}\end{bmatrix} \quad (14)$$

where dead-time and switching period are T_d and $T_{sw}(=1/f_{sw})$ respectively. The corresponding state-space model incorporating this dead-time effect can be found in [14] and is as shown in (16)–(19). The parameter k_d in (18) is a result of linearizing (14) around stable operating points and is shown:

$$k_d = \frac{1}{L_i}\frac{T_d}{T_{sw}}\frac{2\sqrt{6}}{\pi}\frac{1}{\left(I_{id}^2+I_{iq}^2\right)^{3/2}} \quad (15)$$

where i_{idq}, i_{gdq}, v_{idq}, v_{cdq}, and v_{dc}^{out} remain as previously described and their corresponding steady-state values are I_{idq}, I_{gdq}, V_{idq}, V_{cdq}, and V_{dc}^{out} respectively. d-q components of the VSC's grid-bus voltage at the Point of Common Coupling (PCC) and its corresponding steady-state value are v_{gdq} and V_{gdq} respectively. The nominal frequency operating point is ω_n. The LCL filter parameters L_i and R_i, C_f and R_f, and R_g and L_g model VSC-side inductance, filter capacitance, and grid-bus-side inductance respectively as shown in Fig. 3.

5) Virtual Impedance

To improve power sharing between interconnected VSCs, a virtual impedance block with a low-pass filter is included in the control loop between power and voltage controllers. Equivalent derivations on application of virtual impedance $Z_v = R_v + j\omega_n L_v$, including its state-space model can be found in [23] and is shown:

$$[\dot{x}_{lcl}] = A_{lcl}[\Delta x_{lcl}] + B1_{lcl}\begin{bmatrix}\Delta v_{id}\\ \Delta v_{iq}\end{bmatrix} + B2_{lcl}\begin{bmatrix}\Delta v_{gd}\\ \Delta v_{gq}\end{bmatrix} + B3_{lcl}[\Delta\omega_g] \tag{16}$$

$$[\dot{x_{lcl}}] = [\Delta\dot{i}_{id} \quad \Delta\dot{i}_{iq} \quad \Delta\dot{i}_{gd} \quad \Delta\dot{i}_{gq} \quad \Delta\dot{v_{cd}} \quad \Delta\dot{v_{cq}}], \quad [x_{lcl}] = [\Delta i_{id} \quad \Delta i_{iq} \quad \Delta i_{gd} \quad \Delta i_{gq} \quad \Delta v_{cd} \quad \Delta v_{cq}] \tag{17}$$

$$\underbrace{\begin{bmatrix} -\frac{R_i}{L_i} - k_d I_{iq}^2 V_{dc}^{\text{out}} & \omega_n + k_d I_{id} I_{iq} V_{dc}^{\text{out}} & 0 & 0 & -\frac{1}{L_i} & 0 \\ -\omega_n + k_d I_{id} I_{iq} V_{dc}^{\text{out}} & -\frac{R_i}{L_i} - k_d I_{id}^2 V_{dc}^{\text{out}} & 0 & 0 & 0 & -\frac{1}{L_i} \\ 0 & 0 & -\frac{R_g}{L_g} & \omega_n & \frac{1}{L_g} & 0 \\ 0 & 0 & -\omega_n & -\frac{R_g}{L_g} & 0 & \frac{1}{L_g} \\ \frac{1}{C_f} - \frac{R_f R_i}{L_i} - R_f k_d I_{iq}^2 V_{dc}^{\text{out}} & R_f k_d I_{id} I_{iq} V_{dc}^{\text{out}} & \frac{R_f R_g}{L_g} - \frac{1}{C_f} & 0 & -\frac{R_f}{L_i} - \frac{R_f}{L_g} & \omega_n \\ R_f k_d I_{id} I_{iq} V_{dc}^{\text{out}} & \frac{1}{C_f} - \frac{R_f R_i}{L_i} - R_f k_d I_{id}^2 V_{dc}^{\text{out}} & 0 & \frac{R_f R_g}{L_g} - \frac{1}{C_f} & -\omega_n & -\frac{R_f}{L_i} - \frac{R_f}{L_g} \end{bmatrix}}_{A_{lcl}} \tag{18}$$

$$\underbrace{\begin{bmatrix} \frac{1}{L_i} & 0 & 0 & 0 & \frac{R_f}{L_i} & 0 \\ 0 & \frac{1}{L_i} & 0 & 0 & 0 & \frac{R_f}{L_i} \end{bmatrix}^{\mathrm{T}}}_{B1_{lcl}}, \quad \underbrace{\begin{bmatrix} 0 & 0 & -\frac{1}{L_g} & 0 & \frac{R_f}{L_g} & 0 \\ 0 & 0 & 0 & -\frac{1}{L_g} & 0 & \frac{R_f}{L_g} \end{bmatrix}^{\mathrm{T}}}_{B2_{lcl}}, \quad \underbrace{[I_{iq} \quad -I_{id} \quad I_{gq} \quad -I_{gd} \quad V_{cq} \quad -V_{cd}]^{\mathrm{T}}}_{B3_{lcl}} \tag{19}$$

$$\begin{bmatrix}\Delta\dot{i}_{gdf}\\ \Delta\dot{i}_{gqf}\end{bmatrix} = \underbrace{\begin{bmatrix}-\omega_{cvi} & 0\\ 0 & -\omega_{cvi}\end{bmatrix}}_{A_{virt}}\begin{bmatrix}\Delta i_{gdf}\\ \Delta i_{gqf}\end{bmatrix} + \underbrace{\begin{bmatrix}\omega_{cvi} & 0\\ 0 & \omega_{cvi}\end{bmatrix}}_{B_{virt}}\begin{bmatrix}\Delta i_{gd}\\ \Delta i_{gq}\end{bmatrix} \tag{20}$$

$$\begin{bmatrix}\Delta v_{cd}^*\\ \Delta v_{cq}^*\end{bmatrix} = \underbrace{\begin{bmatrix}-R_v & L_v\omega_n\\ L_v\omega_n & -R_v\end{bmatrix}}_{C_{virt}}\begin{bmatrix}\Delta i_{gdf}\\ \Delta i_{gqf}\end{bmatrix} + \underbrace{\begin{bmatrix}1 & 0\\ 0 & 1\end{bmatrix}}_{D1_{virt}}\begin{bmatrix}\Delta v_{cd}^c\\ \Delta v_{cq}^c\end{bmatrix} + \underbrace{\begin{bmatrix}L_v I_{gqf}\\ -L_v I_{gdf}\end{bmatrix}}_{D2_{virt}}[\Delta\omega_g] \tag{21}$$

where virtual resistance and inductance are R_v and L_v respectively. d-q components of injected grid current and its filtered values for virtual impedance loop are i_{gdq} and i_{gdqf} respectively, with corresponding steady-state value $I_{gdqf} = I_{gdq}$. Cut-off frequency of the low-pass filter in the virtual impedance loop is ω_{cvi}, whereas ω_n is the nominal frequency operating point. d-q components of the reference output capacitor voltage and droop-governed command output capacitor voltage are v_{cdq}^* and v_{cdq}^c respectively.

6) Digital Control Emulator (DCE) for VSC

DCE is applied and approximated in a similar way as the boost converter subsystem to all input signals (i_{idq}^*, i_{idq}, and v_{cdq}) to the VSC's current controller.

7) Reference Frame Transformation

In the VSC-MG network, a reference frame transformation is required after declaring one of the VSC's synchronous reference frame as the common D-Q reference frame with frequency $\omega_g = \omega_{gcom}$. The other individual VSCs in the network will be transformed to this common reference frame. Corresponding transformations can be found in [10] and is shown:

$$\begin{bmatrix}\Delta i_{gD}\\ \Delta i_{gQ}\end{bmatrix} = \begin{bmatrix}\cos(\delta_0) & -\sin(\delta_0)\\ \sin(\delta_0) & \cos(\delta_0)\end{bmatrix}\begin{bmatrix}\Delta i_{gd}\\ \Delta i_{gq}\end{bmatrix} + \begin{bmatrix}-I_{gd}\sin(\delta_0) - I_{gq}\cos(\delta_0)\\ I_{gd}\cos(\delta_0) - I_{gq}\sin(\delta_0)\end{bmatrix}[\Delta\delta] \tag{22}$$

$$\begin{bmatrix}\Delta v_{gd}\\ \Delta v_{gq}\end{bmatrix} = \begin{bmatrix}\cos(\delta_0) & \sin(\delta_0)\\ -\sin(\delta_0) & \cos(\delta_0)\end{bmatrix}\begin{bmatrix}\Delta v_{gD}\\ \Delta v_{gQ}\end{bmatrix} + \begin{bmatrix}-V_{gD}\sin(\delta_0) + V_{gQ}\cos(\delta_0)\\ -V_{gD}\cos(\delta_0) - V_{gQ}\sin(\delta_0)\end{bmatrix}[\Delta\delta] \tag{23}$$

where $i_{gdq} \rightarrow i_{gDQ}$ transforms individual VSC's injected grid current in its d-q reference frame to the common D-Q reference frame and $v_{gDQ} \rightarrow v_{gdq}$ transforms the VSC's grid-bus voltage at the PCC from the common D-Q reference frame to the individual d-q reference frame of the VSC. Their corresponding steady-state values are I_{gdq} and V_{gDQ}. The phase angle difference between an individual VSC's reference frame and the common reference frame as previously described is δ and its corresponding steady-state value is δ_0.

C. Linking the Boost Converter and VSC Subsystems

The state-space model with more detailed information characterizing the link between the boost converter and VSC subsystems can be found in [14] and is shown:

$$\begin{bmatrix}\Delta v_{id}\\ \Delta v_{iq}\end{bmatrix} = \underbrace{\begin{bmatrix}D_d\\ D_q\end{bmatrix}}_{C_{Vlink}}[\Delta v_{dc}^{\text{out}}] + \underbrace{\begin{bmatrix}V_{dc}^{\text{out}} & 0\\ 0 & V_{dc}^{\text{out}}\end{bmatrix}}_{D_{Vlink}}\begin{bmatrix}\Delta d_d\\ \Delta d_q\end{bmatrix} \tag{24}$$

$$[\Delta i_{dc}^{\text{out}}] = \frac{3}{2}\underbrace{[D_d \quad D_q]}_{C_{Clink}}\begin{bmatrix}\Delta i_{id}\\ \Delta i_{iq}\end{bmatrix} + \frac{3}{2}\underbrace{[I_{id} \quad I_{iq}]}_{D_{Clink}}\begin{bmatrix}\Delta d_d\\ \Delta d_q\end{bmatrix} \tag{25}$$

where the measured output voltage v_{dc}^{out} from the boost converter is linked to d-q components of the VSC output voltage v_{idq} through the d-q components of the VSC's duty cycle d_{dq}. Additionally, the boost converter's output current i_{dc}^{out} is linked to d-q components of the measured VSC output current i_{idq} by equating the output active power of the VSC with the active power in the DC-link of the boost converter via the principle of power balance on the assumption that the VSC is modeled as a lossless power processor [24]. Steady-state values of the boost converter's measured output voltage and d-q components

$$\begin{bmatrix}\Delta\dot{i}_{lnDab}\\ \Delta\dot{i}_{lnQab}\end{bmatrix}=\underbrace{\begin{bmatrix}-\frac{R_{lnab}}{L_{lnab}} & \omega_n\\ -\omega_n & -\frac{R_{lnab}}{L_{lnab}}\end{bmatrix}}_{A_{lnab}}\begin{bmatrix}\Delta i_{lnDab}\\ \Delta i_{lnQab}\end{bmatrix}+\underbrace{\begin{bmatrix}\frac{1}{L_{lnab}} & 0\\ 0 & \frac{1}{L_{lnab}}\end{bmatrix}}_{B11_{lnab}}\begin{bmatrix}\Delta v_{gDa}\\ \Delta v_{gQa}\end{bmatrix}+\underbrace{\begin{bmatrix}-\frac{1}{L_{lnab}} & 0\\ 0 & -\frac{1}{L_{lnab}}\end{bmatrix}}_{B12_{lnab}}\begin{bmatrix}\Delta v_{gDb}\\ \Delta v_{gQb}\end{bmatrix}+\underbrace{\begin{bmatrix}I_{lnQab}\\ -I_{lnDab}\end{bmatrix}}_{B2_{lnab}}\left[\Delta\omega_{gcom}\right] \tag{26}$$

$$\begin{bmatrix}\Delta\dot{i}_{ldDa}\\ \Delta\dot{i}_{ldQa}\end{bmatrix}=\underbrace{\begin{bmatrix}-\frac{R_{lda}}{L_{lda}} & \omega_n\\ -\omega_n & -\frac{R_{lda}}{L_{lda}}\end{bmatrix}}_{A_{lda}}\begin{bmatrix}\Delta i_{ldDa}\\ \Delta i_{ldQa}\end{bmatrix}+\underbrace{\begin{bmatrix}\frac{1}{L_{lda}} & 0\\ 0 & \frac{1}{L_{lda}}\end{bmatrix}}_{B1_{lda}}\begin{bmatrix}\Delta v_{gDa}\\ \Delta v_{gQa}\end{bmatrix}+\underbrace{\begin{bmatrix}I_{ldQa}\\ -I_{ldDa}\end{bmatrix}}_{B2_{lda}}\left[\Delta\omega_{gcom}\right] \tag{27}$$

of the VSC's duty cycle and measured output current are V_{dc}^{out}, D_{dq}, and I_{idq} respectively.

D. Interconnecting Lines and Loads

Interconnecting lines and loads are described using the generic RL line and RL load respectively; and corresponding state-space models can be found in [10]. For a line connected between adjacent buses a and b, the state-space model is shown in (26), where R_{lnab}, L_{lnab} are line resistance and line inductance respectively. D-Q components of line currents and its corresponding steady-state value are i_{lnDQab} and I_{lnDQab} respectively. D-Q components of network voltages at buses a and b are v_{gDQa} and v_{gDQb} respectively, and corresponds to (23) should both buses have individual VSC connections.

For a load connected at bus a, the state-space model is shown in (27), where R_{lda}, L_{lda} are load resistance and load inductance respectively. D-Q components of the load currents and its corresponding steady-state value are i_{ldDQa} and I_{ldDQa} respectively. Frequencies ω_{gcom} and ω_n remain as previously described. An aggregated state-space model encompassing all interconnecting lines $[i_{LNDQ}]$ and loads $[i_{LDDQ}]$ in the VSC-MG network is shown in (28) and (29) respectively as reported in [10].

$$\begin{aligned}[\Delta\dot{i}_{LNDQ}]=&A_{LN}[\Delta i_{LNDQ}]+B1_{LN}[\Delta v_{gDQ}]\\&+B2_{LN}[\Delta\omega_{gcom}]\end{aligned} \tag{28}$$

$$\begin{aligned}[\Delta\dot{i}_{LDDQ}]=&A_{LD}[\Delta i_{LDDQ}]+B1_{LD}[\Delta v_{gDQ}]\\&+B2_{LD}[\Delta\omega_{gcom}]\end{aligned} \tag{29}$$

where A_{LN}, $B1_{LN}$, and $B2_{LN}$ are coefficient matrices for lines in the network whereas A_{LD}, $B1_{LD}$, and $B2_{LD}$ are identical coefficient matrices for loads in the network.

E. Complete Network Model

Symbolic representation inclusive of interconnections between the VSCs, lines, and loads in the VSC-MG network as illustrated in [10] is shown:

$$\begin{aligned}[\Delta v_{gDQ}]=R_N(&M_{VSC}[\Delta i_{gDQ}]+M_{LN}[\Delta i_{LNDQ}]\\&+M_{LD}[\Delta i_{LDDQ}])\end{aligned} \tag{30}$$

where mapping matrices for VSCs, lines, and loads are M_{VSC}, M_{LN}, and M_{LD} respectively. A sufficiently large virtual resistor (much larger than any other resistance in the network) is applied to each bus in the network through a diagonal matrix R_N to ensure the numerical solution is well conditioned [10]. The complete network state-space model to be analyzed is shown:

$$\begin{bmatrix}\Delta\dot{x}_{BCVSC}\\ \Delta\dot{i}_{LNDQ}\\ \Delta\dot{i}_{LDDQ}\end{bmatrix}=A_{MG}\begin{bmatrix}\Delta x_{BCVSC}\\ \Delta i_{LNDQ}\\ \Delta i_{LDDQ}\end{bmatrix} \tag{31}$$

where x_{BCVSC} contains all associated states in the boost converter and VSC subsystems for all DGs in the VSC-MG network. A_{MG} is the complete system state matrix and is constructed by adopting the graphical modeling approach in [14]. For the ith DG, the state vector is as shown:

$$\begin{aligned}\Delta x_{BCVSCi}=\Delta[&\phi_{bi}\ \ \gamma_{bi}\ \ i_{bi}^{\text{in}}\ \ v_{dci}^{\text{out}}\ \ \delta_i\ \ P_i\ \ Q_i\ \ i_{gdqfi}\\&\phi_{dqi}\ \ \gamma_{dqi}\ \ i_{idqi}\ \ i_{gdqi}\ \ v_{cdqi}]^{\text{T}}\end{aligned} \tag{32}$$

For an individual DG, there are 4 states corresponding to its boost converter subsystem and 15 states corresponding to its VSC subsystem. DCE introduces another 14 states corresponding to the boost converter subsystem and 42 states corresponding to the VSC subsystem. Thus, there are 75 states associated with an individual DG in the VSC-MG network. A third-order *Padé* approximation is used for the linear approximation of the DCE for both subsystems.

III. Small-Signal Stability Analysis on Test VSC-MG Network

The interconnected network shown in Fig. 6 is a 230 V, 50 Hz VSC-MG under study. Each DG representation consists of a DC-DC boost converter and a DC-AC VSC in a two-stage power conversion structure, connected to a network having 6 buses, 6 lines, and 6 loads. Active and reactive power droop gains m_p and n_q govern the supply of power from DGs as the MG network is operating in an islanded mode. The nominal rating for each DG in the network is 100 kVA. The parameters for this MG network including boost and VSC model parameters are presented in Table I. The steady-state initial operating conditions for each DG, similar to [14], are shown in Table II.

The operating condition is with respect to each VSC's droop control characteristics that governs power sharing via m_p and n_q. Each VSC is considered identical for the operating condition in Table II, with the same m_p and n_q, and attempt

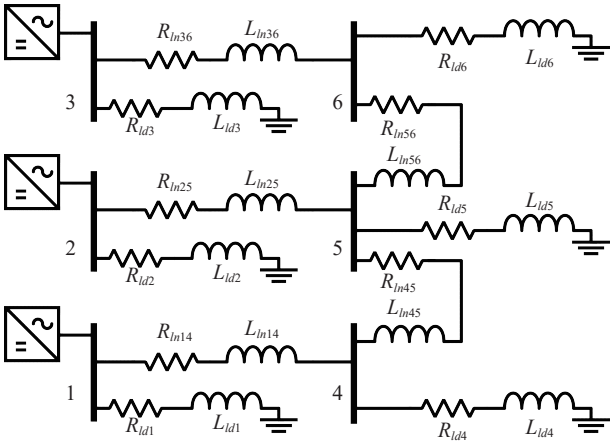

Fig. 6. Test VSC-MG network under study.

TABLE I
NETWORK, BOOST CONVERTER AND VSC MODEL PARAMETERS

Parameter	Value	Parameter	Value	Parameter	Value
V_n	230 V	f_{sw}	10 kHz	T_d	2 μs
ω_n, ω_g	100π rad/s	T_s, T_{pwm}	50 μs	ω_{cpc}, ω_{cvi}	20π rad/s
L_i	6.7238 μH	C_f	350 μF	L_g	6.8 μH
R_i	22.5 mΩ	R_f	210 mΩ	R_g	1 mΩ
m_p	$\pi \times 10^{-6}$	n_q	9×10^{-4}	R_N	10 kΩ
λ_v	1×10^{-4}	λ_c	4×10^{-5}	T_c	5 m*s*
K'_{pv}	5.4978	K'_{iv}	1099.56	K_{pv}	3.5
K'_{pc}	0.0053	K'_{ic}	61.6439	V_b^{in}	540 V
K_{pc}	0.1962	K_{ic}	561.6705	V_{Db}	1.1 V
R_{lb}	1 mΩ	L_{lb}	900 μH	C_{dc}	10 mF
R_{onb}	2 mΩ	K'_{pcb}	0.0206	K'_{icb}	95.3546
Z_{ld5}	(1.6+ j0.5024) Ω	F_V	1	F_C	1
Z_{ld6}	(1.6+ j0.5024) Ω	K'_{pvb}	4.6265	K'_{ivb}	606.0489
Z_{ld1}	(7+ j2.198) Ω	Z_{ld2}	(14+ j4.396) Ω	Z_{ld3}	(4.85+ j1.4444) Ω
Z_{ld4}	(2.4+ j0.7536) Ω	Z_{ln14}	(0.1162+ j0.0233) Ω	Z_{ln25}	(0.1356+ j0.0271) Ω
Z_{ln36}	(0.0969+ j0.0194) Ω	Z_{ln45}	(0.0193+ j0.0091) Ω	Z_{ln56}	(0.0231+ j0.011) Ω
$Z_{v,VSC1}$	(19.6+ j3.9) mΩ	$Z_{v,VSC2}$	(19.6+ j3.9) mΩ	$Z_{v,VSC3}$	(38.7+ j7.8) mΩ

to share interconnected loads equally. Loading conditions are considered moderately heavy with respect to the nominal rating of each DG. This base operating condition is a planning choice and can be varied. Small-signal state-space models described in Section II allows for investigation of small-signal stability for any choice of network parameters and operating conditions. The frequency of DG's VSC at bus 1 sets the common reference frequency, while other VSCs are transformed to this reference frame. The state-space model for the VSC-MG network in Fig. 6 has a total of 247 states. To introduce heterogeneity in the model, virtual impedance of the DG's VSC at bus 2 is set to zero. Thus, in all subsequent analysis, there are a total of 245 states to be investigated. Accompanying results within are obtained with the aid of MATLAB/Simulink R2018b.

A. Eigenvalue Analysis

The eigenvalue analysis reveals the frequency and damping of dominant eigenvalues (modes). Locations of all 245 modes in the VSC-MG network described by matrix $\boldsymbol{A}_{MG}$ are shown in Fig. 7. Each boxed area is zoomed into, in subsequent plots revealing dominant modes in the VSC-MG network. Dominant low frequency modes in boxed area C and some high frequency modes in boxed area B to be analyzed are shown in Table III. Each mode is assigned a number for easier comparison throughout the paper. The contribution of a set of modes towards the overall system performance depends on the proximity of these modes to the right half of the complex plane. The nearer it is, the larger its contribution.

B. Participation Factor Analysis

The participation factor analysis reveals sensitivity of different eigenvalues (modes) to states. This mapping between states and modes help identify critical parameters in the VSC-MG network. It was established in [10] through PI-based control, that the low frequency dominant modes were largely sensitive to states of the VSC's power controller. IMC-based control was compared with PI-based control in [9] and revealed similar findings but showed better eigenvalue patterns thereby yielding improved transient response and increased stability margins. Additionally, it was also established in [12] that high frequency modes were largely sensitive to DCE which models the transport delay for the VSC. These investigations neglected the impact of the boost converter subsystem. The sensitivity of the modes to parameters in the boost converter is therefore investigated.

The participation factor analysis for certain modes of interest is shown in Table III. States with participation factors ≤ 0.015 are not shown. Resulting analysis is consistent with results presented in [10] for low frequency modes and [12] high frequency modes. States introduced by the DCE for both the boost converter and VSC subsystems that have participation factors ≥ 0.005 influenced approximately 15.51% of modes in the high frequency range (> 10000 rad/s). Most modes presented in Table III are largely sensitive to states of the VSC's power controller, particularly m_1–m_{22}^{21}. Within this group of modes are m_{18}^{17}–m_{22}^{21} with some influence from states of the boost converter's power model. Dominant oscillatory modes m_{24}^{23}–m_{28}^{27} in the high frequency range can also be seen to be largely sensitive to states of the boost converter's power model. Also seen are a few modes with little influence from states of the VSC's virtual impedance loop and LCL filter.

To characterize small-signal stability of the VSC-MG network, sensitivity of dominant oscillatory modes to changes in parameters of the boost converter subsystem is investigated. Parameters of interest are R_{lb}, L_{lb}, and R_{onb} as they facilitate excitation of the oscillatory modes $m_{18}^{17}(-165.81 \pm \text{j}132.05)$, $m_{20}^{19}(-166.96 \pm \text{j}132.45)$, $m_{22}^{21}(-163.41 \pm \text{j}135.08)$, $m_{24}^{23}(-72.70 \pm \text{j}17073)$, $m_{26}^{25}(-72.38 \pm \text{j}17074)$, and $m_{28}^{27}(-72.55 \pm \text{j}17075)$ where the state i_{bi}^{in} have comparably high participation factors. The frequency of oscillation for modes m_{18}^{17}, m_{20}^{19}, and m_{22}^{21} are 21.02 Hz, 21.08 Hz, and 21.50 Hz with corresponding damping ratios 78.22%, 78.34%, and 77.08% respectively. Whereas frequency of oscillation for modes m_{24}^{23}, m_{26}^{25}, and m_{28}^{27} are 2717.25 Hz, 2717.41 Hz, and 2717.57 Hz with corresponding damping ratios 0.426%, 0.424%, and 0.425% respectively. The trajectory

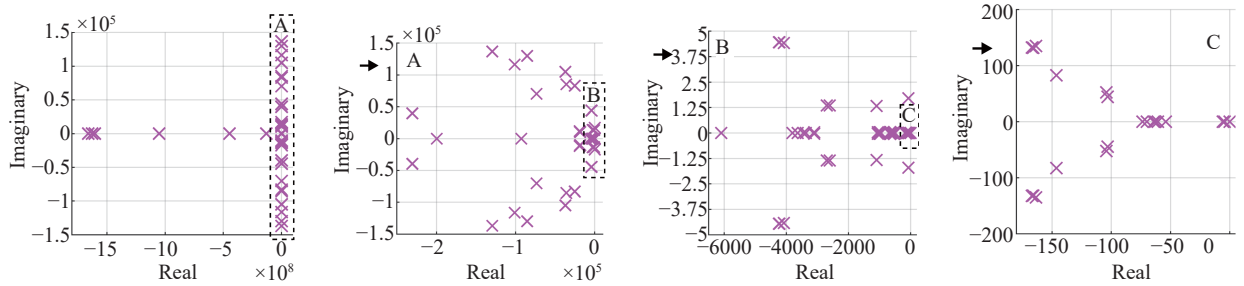

Fig. 7. Locus of eigenvalues for test VSC-MG under study.

TABLE II
STEADY-STATE INITIAL OPERATING CONDITIONS

Parameter	Value	Parameter	Value
δ_{01}	0 rad	V_{cd1}, V_{cd2}, V_{cd3}	[299, 304, 295] V
δ_{02}	-3.88×10^{-4} rad	V_{cq1}, V_{cq2}, V_{cq3}	[0.5, 0, 1] V
δ_{03}	-3.3×10^{-3} rad	I_{id1}, I_{id2}, I_{id3}	[180, 177, 182] A
V_{gD1}, V_{gD2}, V_{gD3}	[296, 302, 292] V	I_{iq1}, I_{iq2}, I_{iq3}	$-$[51, 45, 52] A
V_{gQ1}, V_{gQ2}, V_{gQ3}	[3, 3, 3] V	I_{gd1}, I_{gd2}, I_{gd3}	[179, 175, 181] A
V_{dc1}^{out}, V_{dc2}^{out}, V_{dc3}^{out}	[800] V	I_{gq1}, I_{gq2}, I_{gq3}	$-$[57, 51, 58] A
I_{b1}^{in}, I_{b2}^{in}, I_{b3}^{in}	[148] A	D_{b1}, D_{b2}, D_{b3}	[0.326]
D_{d1}, D_{d2}, D_{d3}	[0.375, 0.381, 0.37]	D_{q1}, D_{q2}, D_{q3}	[0.0175]
P_1, Q_1	[80.9, 24.5] kVA	P_2, Q_2	[80.9, 23.7] kVA
P_3, Q_3	[80.9, 26.5] kVA	I_{ldD1}, I_{ldQ1}	[39, $-$12] A
I_{lnD14}, I_{lnQ14}	[141, $-$42] A	I_{ldD2}, I_{ldQ2}	[19.6, $-$6] A
I_{lnD25}, I_{lnQ25}	[156, $-$42] A	I_{ldD3}, I_{ldQ3}	[55, $-$16] A
I_{lnD36}, I_{lnQ36}	[127, $-$40] A	I_{ldD4}, I_{ldQ4}	[106, $-$31] A
I_{lnD45}, I_{lnQ45}	[34.5, $-$11] A	I_{ldD5}, I_{ldQ5}	[159, $-$47] A
I_{lnD56}, I_{lnQ56}	[32, $-$6] A	I_{ldD6}, I_{ldQ6}	[158, $-$47] A

TABLE III
PARTICIPATION FACTOR ANALYSIS FOR MODES OF INTEREST

$m_{\#}$	Mode	State (Participation)
m_1	-4.65	P_3 (0.374), P_1 (0.333), Q_3 (0.119), Q_1 (0.103), P_2 (0.047), Q_2 (0.013)
m_2	-5.96	P_2 (0.392), P_1 (0.230), P_3 (0.152), Q_2 (0.108), Q_1 (0.065), Q_3 (0.044)
m_3	-62.80	Q_3 (0.972), i_{gdf3} (0.022)
m_4	-62.80	Q_1 (0.655), Q_3 (0.303), i_{gdf1} (0.029)
m_5	-62.75	P_3 (0.330), P_1 (0.328), P_2 (0.313), Q_3 (0.018)
m_6	-60.79	P_3 (0.436), P_1 (0.386), P_2 (0.111), Q_3 (0.042), Q_1 (0.021)
m_7	-64.07	P_1 (0.490), P_2 (0.421), P_3 (0.061), Q_1 (0.020)
m_8	-53.96	P_2 (0.493), P_1 (0.313), P_3 (0.131), Q_2 (0.025), Q_1 (0.023), Q_3 (0.013)
m_9	-69.89	P_3 (0.367), P_1 (0.341), P_2 (0.223), Q_3 (0.037), Q_2 (0.020)
m_{10}	-73.62	P_2 (0.334), P_1 (0.280), P_3 (0.140), Q_2 (0.091), Q_1 (0.079), Q_3 (0.075)
m_{12}^{11}	$-103.05\pm$j44.58	P_2 (0.393), P_1 (0.285), P_3 (0.120), Q_2 (0.094), Q_1 (0.070), Q_3 (0.027)
m_{14}^{13}	$-104.21\pm$j52.23	P_3 (0.408), P_1 (0.296), P_2 (0.102), Q_3 (0.091), Q_1 (0.069), Q_2 (0.022)
m_{16}^{15}	$-146.39\pm$j82.73	P_1 (0.253), P_2 (0.253), P_3 (0.244), Q_1 (0.075), Q_2 (0.075), Q_3 (0.073)
m_{18}^{17}	$-165.81\pm$j132.05	Q_3 (0.359), Q_1 (0.225), Q_2 (0.133), P_3 (0.092), P_1 (0.057), P_2 (0.033), i_{b3}^{in} (0.031), i_{b1}^{in} (0.019)
m_{20}^{19}	$-166.96\pm$j132.45	Q_2 (0.335), Q_1 (0.277), P_2 (0.116), P_1 (0.098), Q_3 (0.061), i_{b2}^{in} (0.027), i_{b1}^{in} (0.023), P_3 (0.021)
m_{22}^{21}	$-163.41\pm$j135.08	P_2 (0.190), P_1 (0.187), P_3 (0.179), Q_2 (0.074), Q_1 (0.064), i_{b2}^{in} (0.062), i_{b1}^{in} (0.061), i_{b3}^{in} (0.057), Q_3 (0.045), v_{dc2}^{out} (0.021), v_{dc1}^{out} (0.020), v_{dc3}^{out} (0.020)
m_{24}^{23}	$-72.70\pm$j17073	i_{b2}^{in} (0.348), i_{b1}^{in} (0.277), i_{b3}^{in} (0.253), i_{id2} (0.017)
m_{26}^{25}	$-72.38\pm$j17074	i_{b1}^{in} (0.412), i_{b2}^{in} (0.379), i_{b3}^{in} (0.066), i_{id1} (0.019), i_{id2} (0.017)
m_{28}^{27}	$-72.55\pm$j17075	i_{b3}^{in} (0.468), i_{b1}^{in} (0.223), i_{b2}^{in} (0.165), i_{id3} (0.021)

of these modes as functions of R_{lb}, L_{lb}, and R_{onb} are shown in Figs. 8, 9, and 10 respectively. The traces of both clusters, m_{18}^{17}, m_{20}^{19}, m_{22}^{21} and m_{24}^{23}, m_{26}^{25}, m_{28}^{27}, overlap each other as they move through the complex plane.

Figure 8 shows that as R_{lb} increases, damping ratio of modes m_{24}^{23}, m_{26}^{25}, and m_{28}^{27} begin increasing as they move further towards the left of the complex plane. However, the damping ratio of modes m_{18}^{17}, m_{20}^{19}, and m_{22}^{21} begin decreasing as they move further towards the right of the complex plane, and thus leads to instability. In Fig. 9, it is shown that as L_{lb} increases, the damping ratio of modes m_{24}^{23}, m_{26}^{25}, and m_{28}^{27} begin decreasing as they move into the right half of the complex plane, hence leading to instability. But as L_{lb} continues to increase, these modes begin returning to the left of the complex plane with increasing damping ratio. However, the damping ratio of modes m_{18}^{17}, m_{20}^{19}, and m_{22}^{21} begin increasing as they move further towards the left of the complex plane. By increasing R_{onb} as shown in Fig. 10, the damping ratio of modes m_{24}^{23}, m_{26}^{25}, and m_{28}^{27} begin increasing as they move towards the left of the complex plane. But as R_{onb} continues

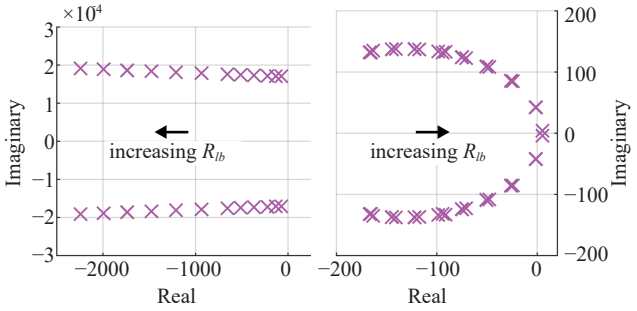

Fig. 8. Mode trajectories as a function of R_{lb}. Left (1 mΩ $\leq R_{lb} \leq$ 4 Ω for m_{24}^{23}, m_{26}^{25}, m_{28}^{27}), Right (1 mΩ $\leq R_{lb} \leq$ 3.6425 Ω for m_{18}^{17}, m_{20}^{19}, m_{22}^{21}).

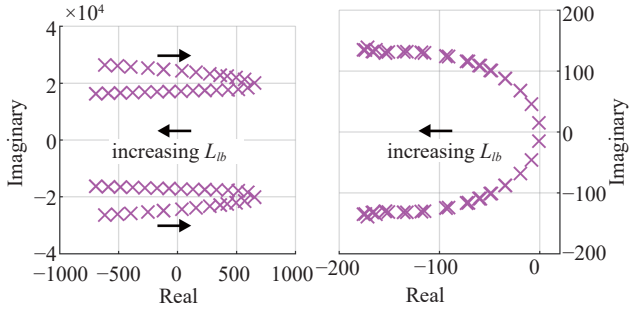

Fig. 9. Mode trajectories as a function of L_{lb}. Left (150 nH $\leq L_{lb} \leq$ 1.8 mH for m_{24}^{23}, m_{26}^{25}, m_{28}^{27}), Right (3 nH $\leq L_{lb} \leq$ 1.8 mH for m_{18}^{17}, m_{20}^{19}, m_{22}^{21}).

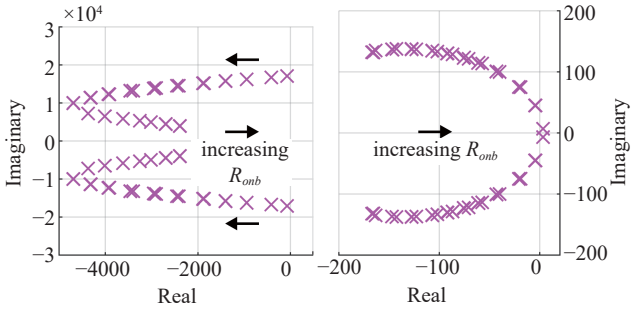

Fig. 10. Mode trajectories as a function of R_{onb}. Left (2 mΩ $\leq R_{onb} \leq$ 4 Ω for m_{24}^{23}, m_{26}^{25}, m_{28}^{27}), Right (2 mΩ $\leq R_{onb} \leq$ 3.646 Ω for m_{18}^{17}, m_{20}^{19}, m_{22}^{21}).

to increase, these modes begin returning to the right of the complex plane with decreasing damping ratio. However, the damping ratio of modes m_{18}^{17}, m_{20}^{19}, and m_{22}^{21} begin decreasing as they move further towards the right of the complex plane, and thus leads to instability.

C. Analyzing Different Operating Conditions

Small-signal stability is almost independent of operating condition and the effect of the operating condition on dominant modes is minor [25]–[27]. Six different operating conditions (OCs) shown in Table IV are investigated and their corresponding mode locations are presented in Table V. Parameters changed are with respect to base parameters in Table I. OC 1 is an attempt to reach full loading on the DGs in which the power outputs are increased consequently. OC 2 sees a reduction in load and hence a reduction in DG power outputs. OC 3 and OC 4 uses dissimilar active and reactive power droop gains m_p and n_q respectively resulting in different DG power outputs. In OC 3, droop control characteristics shows an increase in active power output for the DG's VSC with the smaller m_p and a decrease in active power output for the DG's VSC with larger m_p. A similar analogy can be inferred in OC 4 between reactive power output and n_q. OC 5 and OC 6 uses higher m_p and n_q respectively. In OC 5, a consequence of a higher m_p is a reduction in steady-state operating network frequency, whereas in OC 6, a consequence of a higher n_q is a reduction in output voltage of the VSCs and hence active and reactive power outputs.

In Table V, the same modes m_1–m_{28}^{27} in Table III, remain dominant modes and are critical for different operating conditions. In the likelihood that new dominant modes appear for a different initial operating condition, a new participation factor analysis would be required to determine states these new dominant modes are sensitive to. New dominant modes remain largely sensitive to states of VSC's power controller

TABLE IV
DIFFERENT OPERATING CONDITIONS

OC	DG power outputs	Parameters changed
1	P_1, P_2, P_3 [92.11, 92.10, 92.12] kW	Network Load
	Q_1, Q_2, Q_3 [27.93, 26.98, 29.98] kvar	Increased by 15%
2	P_1, P_2, P_3 [76.29, 76.28, 76.29] kW	Network Load
	Q_1, Q_2, Q_3 [23.17, 22.35, 24.99] kvar	Decreased by 7.5%
3	P_1, P_2, P_3 [88.19, 80.52, 74.25] kW	m_{p1}, m_{p2}, m_{p3}
	Q_1, Q_2, Q_3 [22.16, 23.81, 28.82] kvar	[0.9, 1, 1.1] $\times\pi\times10^{-6}$
4	P_1, P_2, P_3 [80.96, 80.96, 80.95] kW	n_{q1}, n_{q2}, n_{q3}
	Q_1, Q_2, Q_3 [26.82, 23.63, 24.32] kvar	[0.9, 1, 1.1] $\times9\times10^{-4}$
5	P_1, P_2, P_3 [80.94, 80.94, 80.94] kW	m_{p1}, m_{p2}, m_{p3}
	Q_1, Q_2, Q_3 [24.49, 23.67, 26.53] kvar	[2, 2, 2] $\times\pi\times10^{-6}$
6	P_1, P_2, P_3 [71.87, 71.88, 71.89] kW	n_{q1}, n_{q2}, n_{q3}
	Q_1, Q_2, Q_3 [21.95, 21.54, 22.91] kvar	[2, 2, 2] $\times9\times10^{-4}$

TABLE V
MODE ANALYSIS AT DIFFERENT OPERATING CONDITIONS

$m_\#$	OC 1	OC 2	OC 3	OC 4	OC 5	OC 6
m_1	−4.50	−4.76	−4.66	−4.71	−10.71	−5.64
m_2	−5.79	−6.12	−5.98	−6.00	−15.68	−7.31
m_3	−62.80	−62.80	−62.80	−62.80	−62.80	−62.80
m_4	−62.80	−62.80	−62.80	−62.80	−62.80	−62.80
m_5	−62.75	−62.76	−62.75	−62.75	−62.71	−62.76
m_6	−60.68	−60.77	−60.76	−60.72	−54.02	−60.72
m_7	−64.27	−63.97	−64.13	−64.07	−63.83	−64.09
m_8	−54.27	−53.77	−54.13	−53.99	−39.73	−54.21
m_9	−70.49	−69.57	−69.69	−69.62	−66.44	−69.86
m_{10}	−75.35	−72.94	−73.56	−73.69	−73.87	−83.12
m_{12}^{11}	−101.17 ±j44.97	−100.41 ±j44.83	−100.76 ±j44.85	−100.67 ±j44.21	−103.20 ±j45.74	−105.19 ±j57.31
m_{14}^{13}	−102.63 ±j52.47	−101.35 ±j52.28	−101.83 ±j52.29	−101.87 ±j52.85	−103.80 ±j52.50	−106.79 ±j62.74
m_{16}^{15}	−146.78 ±j81.66	−146.18 ±j82.93	−146.36 ±j82.57	−146.36 ±j82.56	−146.36 ±j82.56	−146.29 ±j82.44
m_{18}^{17}	−166.69 ±j132.25	−164.54 ±j131.40	−164.59 ±j131.49	−166.30 ±j132.04	−165.16 ±j131.64	−172.65 ±j135.55
m_{20}^{19}	−168.10 ±j132.59	−165.82 ±j131.65	−167.02 ±j132.18	−165.43 ±j131.51	−166.51 ±j131.94	−173.09 ±j136.27
m_{22}^{21}	−165.44 ±j136.06	−163.57 ±j134.75	−164.20 ±j135.05	−164.12 ±j135.13	−164.11 ±j135.13	−163.23 ±j134.47
m_{24}^{23}	−193.94 ±j16928	−65.48 ±j17084	−159.21 ±j16970	−102.42 ±j17039	−101.19 ±j17041	−31.29 ±j17126
m_{26}^{25}	−188.84 ±j16933	−61.84 ±j17088	−95.41 ±j17047	−99.67 ±j17043	−100.13 ±j17042	−29.00 ±j17128
m_{28}^{27}	−187.67 ±j16934	−61.18 ±j17089	−46.96 ±j17106	−98.37 ±j17044	−98.68 ±j17043	−28.24 ±j17129

and the boost converter's power model. From the viewpoint of stability, R_{lb}, L_{lb}, and R_{onb} are therefore critical parameters that shape trajectories of some of the dominant oscillatory modes in the VSC-MG network. Stability at both terminals of the VSC subsystem is not equivalent. There is therefore a need to optimize boost converter parameters for cases where, although the AC terminal of the VSC subsystem seems stable, the DC terminal might be unstable.

D. Preliminary Simulation Results

The VSC-MG network is represented using the state-space model and its accompanying dynamic response is implemented using Simulink to validate the analysis performed in subsections III-A and III-B. Simulation results presented within include start-up transient behavior and the (doubling) step change in the load at bus 6 at time = 1.0 s. This doubled load is considered large enough to capture the high frequency modes dominated by states of the boost converter's power model. The figures within this subsection illustrate stable responses at the AC terminal of the VSC subsystem with the same R_{lb}, L_{lb}, and R_{onb} presented in Table I. The response of the active and reactive power outputs from DGs is shown in Fig. 11. The VSC's droop control-based power controller in conjunction with the virtual impedance loop governs the equal and improved sharing of active (P) and reactive (Q) power loads between the DGs. The closest DG electrically to the change in load, responds faster than other DGs and picks up most of this change in load initially. In this case, the DG at bus 3 is the closest electrically to change in load, followed by the DG at bus 2, and then the DG at bus 1. Steady-state values after the change in load are $P_{1,2,3}$ [98.7, 98.7, 98.8] kW and $Q_{1,2,3}$ [28.5, 28.9, 33.5] kvar.

The response of d-q components of output VSC currents i_{idq} and injected grid currents i_{gdq} from DGs is shown in Figs. 12 and 13 respectively. d- component of both currents would respond in a similar manner to active power sharing, whereas q- component of both currents would respond in a similar manner to reactive power sharing, during the step change in load. The steady-state values after the change in load are $i_{id1,2,3}$ [224, 221, 232] A, $i_{iq1,2,3}$ [−9, −9, −13] A, $i_{gd1,2,3}$ [223, 220, 231] A, and $i_{gq1,2,3}$ [−64, −64, −77] A. The response of the d-q components of the output capacitor voltages v_{cdq} from the DGs is shown in Fig. 14. The d- component responds inversely to the reactive power sharing between the DGs. Steady-state values after the change in load are $v_{cd1,2,3}$ [295, 299, 286] V and $v_{cq1,2,3}$ [0.4, 0, 1.2] V. The response of the droop-governed VSC frequency from the DGs is shown in Fig. 15, where each VSC's droop-governed frequency responds inversely to active power sharing between the DGs. DG at bus 3 being the closest electrically to the change in load would experience a wider swing of its droop-governed frequency compared to the DG at bus 2, and then followed by the DG at bus 1. The steady-state network frequency after the change in load is 313.85 rad/s.

IV. Boost Converter Parameter Optimization

A. Particle Swarm Optimization (PSO)

An optimization framework utilizing PSO is developed in this Section to mitigate effects of the boost converter param-

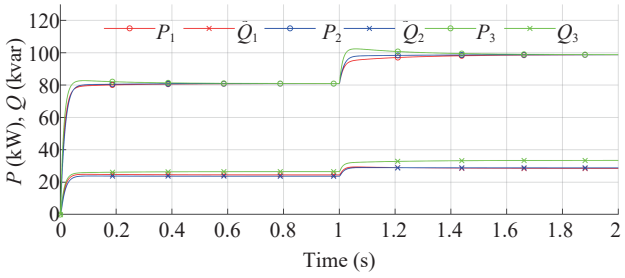

Fig. 11. Active and reactive power outputs from DGs.

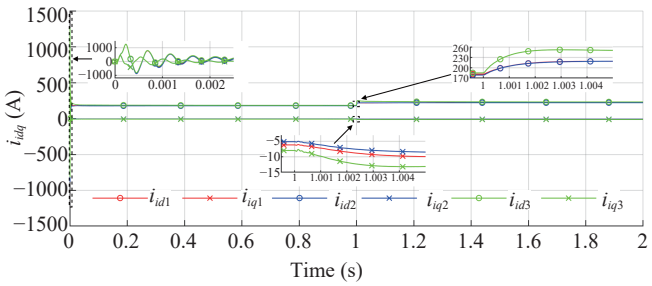

Fig. 12. Output VSC currents from DGs.

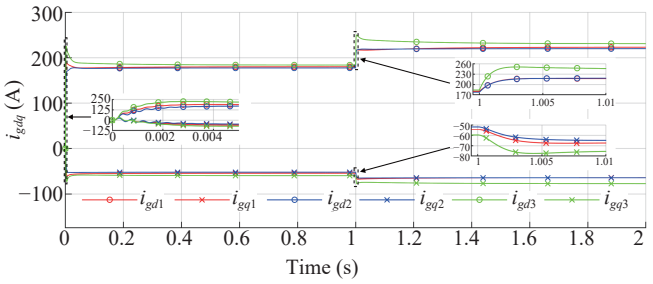

Fig. 13. Injected grid currents from DGs.

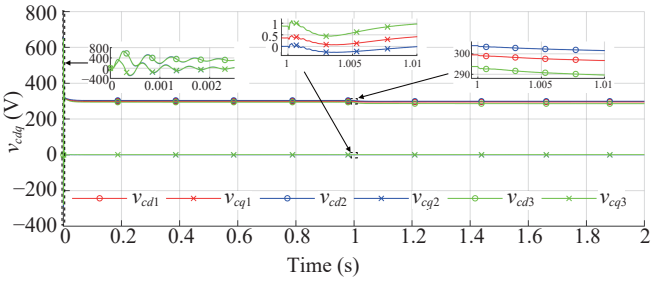

Fig. 14. Output capacitor voltages from DGs.

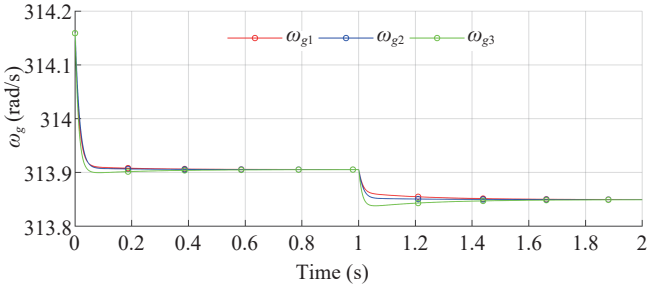

Fig. 15. Droop-governed VSC frequency from DGs.

eters R_{lb}, L_{lb}, and R_{onb}, with regards to instability that could arise from the DC terminal of the VSC subsystem. Selection of these parameters for a satisfactory transient response is the desired outcome. PSO is an evolutionary computation technique inspired by social behavior of bird flocking, fish schooling, and swarming theory [28]. It is the preferred tool to be used due to its precision of solutions, simplicity of tuning parameters, enhanced global search, and convergence capability [29]. The performance of PSO depends on movement of each particle and cooperation of the swarm. Three distinct features include the best fitness of each particle, best fitness of the swarm, and velocity and position update of each particle. Each particle in the swarm starts at a random position and searches the space using its own best knowledge and the swarm's best experience. Movement of the particles in the optimization framework developed is given as shown:

$$w^k = w_{\max} - (w_{\max} - w_{\min}) \cdot ((k-1)/N) \tag{33}$$

$$V_i^{k+1} = w^k V_i^k + c_1 r_1 (Xpb_i^k - X_i^k) + c_2 r_2 (Xsb^k - X_i^k) \tag{34}$$

$$X_i^{k+1} = X_i^k + V_i^{k+1} \tag{35}$$

where i, N, and k are the particle, the total number of iterations set to 100, and iteration index respectively. Swarm size p_s, which is the total number of particles in the swarm is set to 10. The inertia weight at iteration k is w^k which linearly decreases from $w_{\max}$ to $w_{\min}$ with settings 0.9 to 0.4 respectively. The velocity and position vectors at iteration k for each particle i are V_i^k and X_i^k respectively. Constants c_1, c_2 are positive numbers set to 2, and r_1, r_2 are two uniformly distributed random numbers in the range $[0,1]$. The best positions each particle i has attained so far based on its own knowledge and the swarm's best experience are Xpb_i^k and Xsb^k respectively.

B. Optimization Framework

The optimization framework developed considers dynamic coupling through a non-ideal DC-link voltage terminal between the boost converter and VSC subsystems. The objective of optimizing the boost converter parameters R_{lb}, L_{lb}, and R_{onb} is to mitigate their effects with regards to instability that could arise from the DC terminal of the VSC subsystem. Analysis deduced from Table III and Figs. 8–10 show by maximizing horizontal distance between the real part of the dominant mode(s) more sensitive to boost converter parameters and real part of the dominant mode(s) more sensitive to parameters of the VSC subsystem, the effect of boost converter parameters on instability that could arise from the DC terminal of the VSC subsystem would be mitigated. In other words, dynamics from the boost converter subsystem would decay rapidly at the DC terminal of the VSC subsystem, when dominant mode(s) that are more sensitive to boost converter parameters are moved further to the left of the complex plane. Consequently, this results in improved damping ratios for these mode(s). The objective function to be maximized can be expressed as shown:

$$\max J = \text{Real}\{\lambda_{v_{sys}}\} - \text{Real}\{\lambda_{b_{sys}}\} \tag{36}$$

where v_{sys} and b_{sys} are subsets of all modes in the overall system that are more sensitive to parameters of the VSC and boost converter subsystems respectively.

Dominant mode(s) in the VSC v_{sys} and boost converter b_{sys} subsystems are $\lambda_{v_{sys}}$ and $\lambda_{b_{sys}}$ respectively. In this study, if a mode has participation factors ≥ 0.1, from states belonging to the VSC and boost converter subsystems, that mode is included in b_{sys} and used as a limiting factor in evaluating (36). For example, if a mode m_y^x appears during the optimization process with state (participation) of Q_1 (0.15) and i_{b3}^{in} (0.1), from VSC and boost converter subsystems respectively, that mode m_y^x is included in b_{sys}. This is the preferred approach to mitigate the effects of the boost converter subsystem on stability considering the plug-and-play capability for VSCs in MG networks is better suited towards the power controller of the VSC subsystem. Parameters associated with the VSC subsystem are not included in the optimization framework.

To improve computational efficiency of the optimization framework, the domain of stability for $R_{lb} \in$ [1 mΩ, 3.5 Ω], $L_{lb} \in$ [800 μH, 8.43 mH], and $R_{onb} \in$ [2 mΩ, 3.622 Ω], obtained from mode trajectories shown in Figs. 8, 9, and 10 respectively are selected as the constraints of the optimization. Each particle's position $X_i = (R_{lb}, L_{lb}, R_{onb})$ contain the parameters to be optimized. Three conditions are incorporated to define boundaries for the search space and ensure every particle's position results in a stable outcome. These conditions must be performed after the velocity and position update of each particle at every iteration to facilitate the convergence of the swarm:

1) Upper and lower limits, $X_{i,j}^{\max}$ and $X_{i,j}^{\min}$ with regards to the domain of stability for the jth element of the ith particle's position $X_{i,j}$

$$\begin{gathered} X_{i,j}^{\max} = \max[X_{i,j}],\ X_{i,j}^{\min} = \min[X_{i,j}] \\ \text{if}\ \ X_{i,j}^k > X_{i,j}^{\max},\ \text{then}\ \ X_{i,j}^k = X_{i,j}^{\max} \\ \text{else if}\ \ X_{i,j}^k < X_{i,j}^{\min},\ \text{then}\ \ X_{i,j}^k = X_{i,j}^{\min} \end{gathered} \tag{37}$$

2) Upper and lower limits, $V_i^{\max}$ and $V_i^{\min}$ with regards to the jth element of the ith particle's velocity $V_{i,j}$

$$\begin{gathered} V_{i,j}^{\max} = 0.2\left(X_{i,j}^{\max} - X_{i,j}^{\min}\right),\ V_{i,j}^{\min} = -V_{i,j}^{\max} \\ \text{if}\ \ V_{i,j}^k > V_{i,j}^{\max},\ \text{then}\ \ V_{i,j}^k = V_{i,j}^{\max} \\ \text{else if}\ \ V_{i,j}^k < V_{i,j}^{\min},\ \text{then}\ \ V_{i,j}^k = V_{i,j}^{\min} \end{gathered} \tag{38}$$

3) If an unstable mode appears with regards to the jth element of the ith particle's position $X_{i,j}$, replace the element having a higher percentile in its domain with its corresponding $X_{i,j}^{\min}$ till all modes in the overall system are stable using the example as shown:

$$\begin{aligned} \text{assume}\ X_{i,j}^k &= (X_{i,R_{lb}}^k, X_{i,L_{lb}}^k, X_{i,R_{onb}}^k)@(45,5,70)\% \\ &\xrightarrow{\text{unstable?}} (X_{i,R_{lb}}^k, X_{i,L_{lb}}^k, X_{i,R_{onb}}^{\min}) \\ &\xrightarrow{\text{unstable?}} (X_{i,R_{lb}}^{\min}, X_{i,L_{lb}}^k, X_{i,R_{onb}}^{\min}) \\ &\xrightarrow{\text{unstable?}} (X_{i,R_{lb}}^{\min}, X_{i,L_{lb}}^{\min}, X_{i,R_{onb}}^{\min}) \end{aligned} \tag{39}$$

where $X_{i,R_{lb}}^{\min}$, $X_{i,L_{lb}}^{\min}$, and $X_{i,R_{onb}}^{\min}$ for boost converter parameters resulted in a stable outcome as extrapolated from Figs. 8–10. The complete optimization framework using PSO is described using the following steps:

1) *Initialization*:

1.1 In the swarm of size p_s, randomly select each particle's position $X_{i,j}$ within the domain of stability.
1.2 Initialize each particle's velocity $V_{i,j}$ to 0.
1.3 Evaluate overall system modes while adhering to (39) for each particle.
1.4 Evaluate J using (36) for each particle. Xpb_i is initialized with a copy of X_i . Xsb is initialized with a copy of X_i having the best J.

2) *Iteration & Weight Update*: With k starting at 1, update the iteration index. Update inertia weight using (33).

3) *Velocity Update*: Update each particle's velocity using (34). Then apply (38) to ensure all velocities are within predefined limits.

4) *Position Update*: With updated velocities, each particle's position is updated using (35). Then apply (37) to ensure all positions are within predefined limits.

5) *Unstable Mode Check & Objective Function*: For each particle, evaluate overall system modes while adhering to (39). Then evaluate J using (36) for each particle.

6) *Particle Best Update*: For each particle, if the evaluated J in the current iteration is better than the evaluated J's in previous iterations, then update Xpb_i with a copy of X_i.

7) *Swarm Best Update*: In the current iteration, update Xsb with a copy of Xpb_i having the best J.

8) *Stopping Criteria*: Steps 2 to 7 are repeated until one of the following conditions is met:

8.1 The maximum number of iterations N is reached.
8.2 The evaluated J has not improved for a predefined number of iterations.

C. Results and Discussion

1) Optimization Framework Results

The convergence of the objective function is shown in Fig. 16, and maximized at $J = 4240.346$ using the limiting factor described in subsection IV-B. This limiting factor is used during the optimization process due to growing sensitivity from the boost converter parameters, particularly on modes m_{18}^{17}, m_{20}^{19}, and m_{22}^{21} described in subsection III-B. The resulting optimized boost converter parameters are $R_{lb} = 0.001\ \Omega$, $L_{lb} = 800\ \mu$H, and $R_{onb} = 2.16548\ \Omega$. Four cases with different boost converter parameters shown in Table VI are used to validate results of the optimization framework. Simulation results presented within include start-up transient behavior and the (doubling) step change in the load at bus 6 at time = 1.0 s.

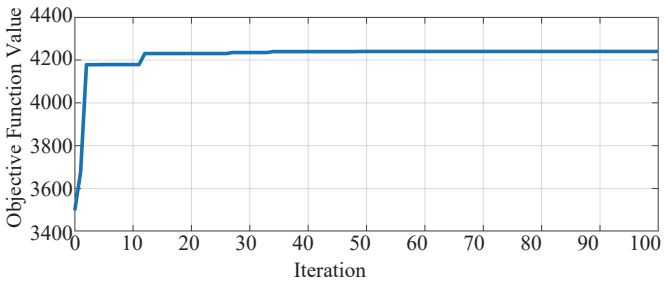

Fig. 16. Objective function convergence.

The response of input currents i_b^{in} and output voltages v_{dc}^{out} from the boost converters are shown in Figs. 17–20. The output DC-link voltage v_{dc}^{out} is shown to not be an ideal constant voltage source for the interfaced VSC subsystem.

TABLE VI
SUMMARY OF CASES

Case	R_{lb} (Ω)	L_{lb} (μH)	R_{onb} (Ω)	$\lambda_{v_{sys}}^{\text{real}}$	$\lambda_{b_{sys}}^{\text{real}}$	J
1	0.001	800	0.002	−4.654	−4.672	0.018
2	0.001	900	0.002	−4.654	−72.375	67.721
3	0.001	800	2.16548	−4.654	−4245	4240.346
4	1.9	1200	1.635	−0.368	0.060	−0.428

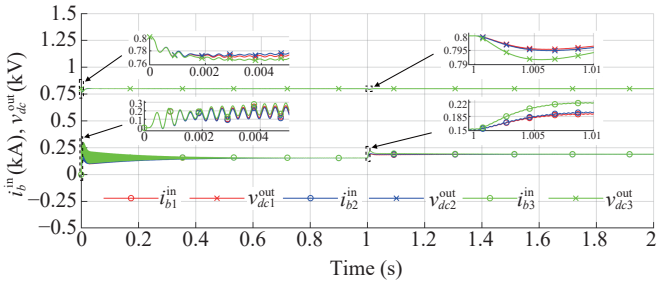

Fig. 17. Input currents, output voltages from boost converters for Case 1.

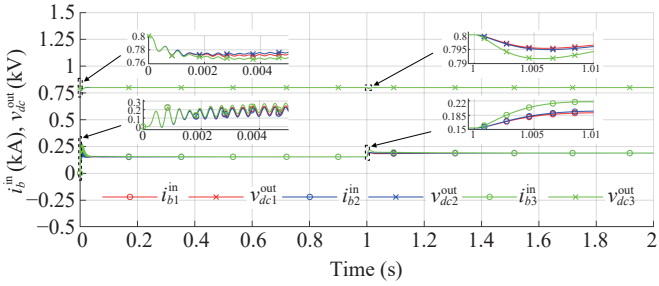

Fig. 18. Input currents, output voltages from boost converters for Case 2.

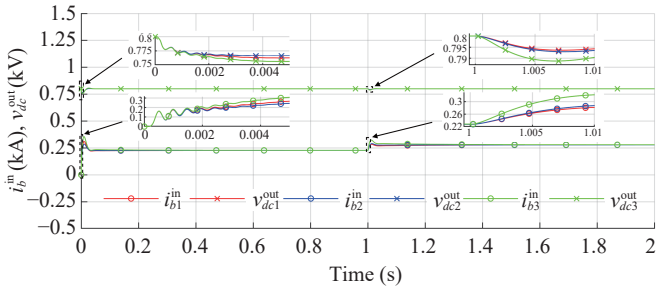

Fig. 19. Input currents, output voltages from boost converters for Case 3.

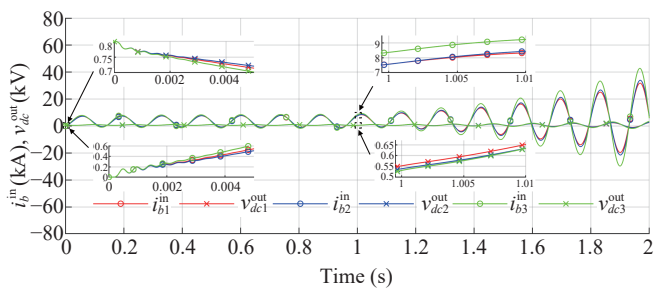

Fig. 20. Input currents, output voltages from boost converters for Case 4.

Corresponding mode locations associated with the boost converter subsystem between the four cases are shown in Table VII. Dominant mode(s) in the VSC and boost converter subsystems from (36), $\lambda_{v_{sys}}$ and $\lambda_{b_{sys}}$ in Table VI, maps to m_1 and m_{26}^{25} for Cases 1 and 2, and to m_1 and m_{24}^{23} for Case 3, and lastly to m_{20}^{19} and m_{18}^{17} for Case 4 as shown in Table VII. The reason for this is in relation to the limiting factor previously described. In subsection III-B, it was shown modes m_{18}^{17}–m_{22}^{21} were largely sensitive to states of the VSC's power controller with some influence from states of the boost converter's power model, whereas modes m_{24}^{23}–m_{28}^{27} in the high frequency range were largely sensitive to states of the boost converter's power model. In Case 4, m_{18}^{17} has a state (participation) of i_{b1}^{in} (0.311), i_{b2}^{in} (0.311), and i_{b3}^{in} (0.298), whereas m_{20}^{19} has a state (participation) of i_{b3}^{in} (0.307), i_{b1}^{in} (0.258), P_3 (0.108), and P_1 (0.095). Also in Case 4, m_{22}^{21} has a state (participation) of i_{b2}^{in} (0.294), i_{b1}^{in} (0.185), i_{b3}^{in} (0.127), and P_2 (0.125). This indicates for Case 4 that modes m_{18}^{17}–m_{22}^{21} are now largely sensitive to states of the boost converter's power model with reduced influence from states of the VSC's power controller.

TABLE VII
BOOST CONVERTER ASSOCIATED MODE LOCATIONS

$m_{\#}$	Case 1	Case 2	Case 3	Case 4
m_1	−4.65	−4.65	−4.65	−4.65
m_{18}^{17}	−164.94 ±j131.73	−165.81 ±j132.05	−116.03 ±j135.14	0.06 ±j46.15
m_{20}^{19}	−166.06 ±j132.12	−166.96 ±j132.45	−120.76 ±j136.21	−0.37 ±j46.33
m_{22}^{21}	−162.54 ±j134.63	−163.41 ±j135.08	−120.95 ±j135.64	−0.40 ±j46.41
m_{24}^{23}	−4.88 ±j17153	−72.70 ±j17073	−4245.0 ±j11904	−4628.4 ±j14118
m_{26}^{25}	−4.67 ±j17154	−72.38 ±j17074	−4258.6 ±j11919	−4626.2 ±j14118
m_{28}^{27}	−4.83 ±j17154	−72.55 ±j17075	−4259.0 ±j11921	−4606.1 ±j14122

2) Impact on Boost Converter Subsystem

Case 1 belongs to the minimum boost converter parameters $X_{i,R_{lb}}^{\min}$, $X_{i,L_{lb}}^{\min}$, and $X_{i,R_{onb}}^{\min}$ in the domain of stability and its corresponding response is shown in Fig. 17. The steady-state values after the change in load are $v_{dc1,2,3}^{\text{out}}$ [800] V and $i_{b1,2,3}^{\text{in}}$ [189] A. The evaluated J for this case is 0.018 with both $\lambda_{v_{sys}}$ and $\lambda_{b_{sys}}$ located close to the right half of the complex plane as shown in Table VI. Case 2 belongs to the base case boost converter parameters used in Section III and its corresponding response is shown in Fig. 18. The steady-state values after the change in load are $v_{dc1,2,3}^{\text{out}}$ [800] V and $i_{b1,2,3}^{\text{in}}$ [189] A. Evaluated J and consequently, settling time after the start-up transient behavior are improved for this case compared to Case 1. The optimized parameters belonging to Case 3 are shown in Fig. 19 to exhibit better overall transient behavior. The steady-state values after the change in load are $v_{dc1,2,3}^{\text{out}}$ [800] V and $i_{b1,2,3}^{\text{in}}$ [279] A. At the maximum J evaluated, $\lambda_{b_{sys}}$ is at its furthest location from the right half of the complex plane, and hence impact from the boost converter subsystem on stability is mitigated. Case 4 belongs to boost converter parameters within the domain of stability and its corresponding response is shown in Fig. 20. Despite being within the domain of stability, the evaluated J for this case is −0.428 with $\lambda_{v_{sys}}$ located close to right half of the complex plane, and an unstable mode $\lambda_{b_{sys}}$ located in the right half of the complex plane as shown in Table VI. This instability from the boost converter subsystem is propagated to the VSC subsystem through the DC-link voltage terminal and results in an unstable overall system. This case illustrates the need to perform stability analysis combining both subsystems due to the dynamic coupling provided at the DC-link voltage terminal.

The response characteristics of the boost converter between the four cases are compared in Table VIII. Measurements include settling time during the period from start-up to change in load t_s^0, settling time after change in load t_s^1, percent overshoot during the period from start-up to change in load M_p^0, and percent overshoot after change in load M_p^1. A reduction in settling time and percent overshoot is a desired objective in improving dynamic performances. This can be seen in Table VIII for t_s^0 and M_p^0 of each boost converter's i_{bi}^{in} when comparing Cases 1, 2, and 3. The equivalence from small-signal analysis is in relation to modes m_{24}^{23}–m_{28}^{27} in Table VII that were largely sensitive to i_{bi}^{in}. There is also slight improvement in t_s^0 of each boost converter's v_{dci}^{out} when comparing Cases 1, 2, and 3. Case 4 presents an unstable mode m_{18}^{17} that is now largely sensitive to i_{bi}^{in}. The desired dynamic performance exhibited by the optimized boost converter parameters R_{lb}, L_{lb}, and R_{onb} belonging to Case 3 cannot be achieved by adjusting the proportional and integral coefficients of the PI-based voltage and current controllers of the boost converter subsystem. Dominant modes are not sensitive to states associated with PI-based voltage and current controllers of the boost converter subsystem, and hence proportional and integral coefficients of both controllers are not considered critical parameters in exciting these modes and shaping their trajectories towards achieving a better dynamic performance.

TABLE VIII
BOOST CONVERTER RESPONSE CHARACTERISTICS

Characteristics		Case 1	Case 2	Case 3	Case 4
v_{dc1}^{out}	t_s^0, t_s^1 (s)	0.13, 1.04	0.04, 1.04	0.04, 1.04	*Uns*,*Uns*
	M_p^0, M_p^1 (%)	0.30, 0.03	0.21, 0.03	0.49, 0.08	*Uns*,*Uns*
i_{b1}^{in}	t_s^0, t_s^1 (s)	0.83, 1.17	0.11, 1.16	0.04, 1.16	*Uns*,*Uns*
	M_p^0, M_p^1 (%)	75.33, 1.40	61.29, 1.10	36.86, 1.69	*Uns*,*Uns*
v_{dc2}^{out}	t_s^0, t_s^1 (s)	0.14, 1.04	0.03, 1.04	0.04, 1.04	*Uns*,*Uns*
	M_p^0, M_p^1 (%)	0.17, 0.02	0.07, 0.02	0.27, 0.07	*Uns*,*Uns*
i_{b2}^{in}	t_s^0, t_s^1 (s)	0.81, 1.09	0.09, 1.11	0.03, 1.04	*Uns*,*Uns*
	M_p^0, M_p^1 (%)	63.95, 3.97	49.59, 3.57	26.09, 4.39	*Uns*,*Uns*
v_{dc3}^{out}	t_s^0, t_s^1 (s)	0.10, 1.04	0.04, 1.04	0.04, 1.04	*Uns*,*Uns*
	M_p^0, M_p^1 (%)	0.47, 0.09	0.38, 0.09	0.77, 0.21	*Uns*,*Uns*
i_{b3}^{in}	t_s^0, t_s^1 (s)	0.82, 1.30	0.12, 1.24	0.09, 1.19	*Uns*,*Uns*
	M_p^0, M_p^1 (%)	95.61, 15.10	81.96, 14.93	56.42, 15.58	*Uns*,*Uns*

3) Impact on VSC Subsystem

Figures 21–25 and Figs. 26–30 illustrate dynamic responses at the AC terminal of the VSC subsystem for Cases 3 and 4 respectively with simulation *time* extended to 3.0 s. Case 3 belongs to the optimized boost converter parameters previously shown in Fig. 19 to exhibit better start-up transient behavior at the DC terminal of the VSC subsystem, whereas Case 4 belongs to boost converter parameters within the domain

of stability that resulted in instability at the DC terminal of the VSC subsystem as previously shown in Fig. 20. Despite Figs. 21–25 for Case 3 exhibiting similar dynamic responses at the AC terminal of the VSC subsystem to Figs. 11–15 for Case 2, they both exhibited dissimilar start-up transients at the DC terminal of the VSC subsystem. The resistance of the switching device in its "on-state", R_{onb} in the boost converter subsystem can be considered a more critical parameter in maintaining stability, aiding in damping start-up transients. For Case 3, steady-state values after the change in load are $P_{1,2,3}$ [98.7, 98.7, 98.7] kW, $Q_{1,2,3}$ [28.5, 28.8, 33.5] kvar, $i_{id1,2,3}$ [224, 221, 232] A, $i_{iq1,2,3}$ [−9, −9, −13] A, $i_{gd1,2,3}$ [223, 220, 231] A, $i_{gq1,2,3}$ [−64, −64, −77] A, $v_{cd1,2,3}$ [295, 299, 286] V and $v_{cq1,2,3}$ [0.4, 0, 1.2] V, with network frequency at 313.85 rad/s.

The depiction of instability with Case 4 is shown in Figs. 26–30. Instability from the boost converter subsystem previously shown in Fig. 20 propagated to the VSC subsystem through the DC-link voltage terminal and resulted in an unstable overall system. This case indicates inadequate boost converter parameters selected within the domain of stability described in subsection IV-B, highlighting the need for their careful selection. The internal resistance of the input filter inductor, R_{lb} in the boost converter subsystem can be

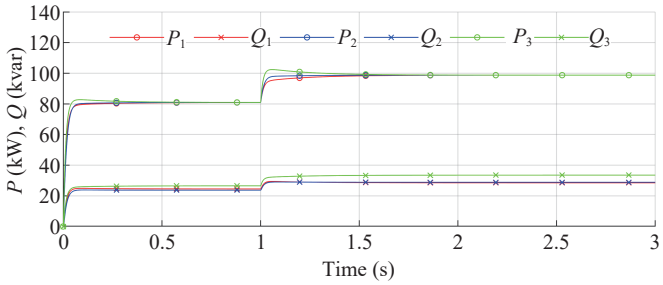

Fig. 21. Active and reactive power outputs from DGs for Case 3.

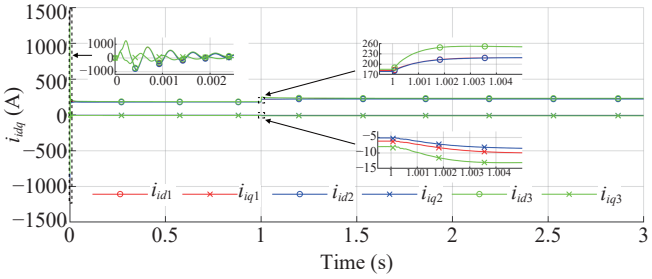

Fig. 22. Output VSC currents from DGs for Case 3.

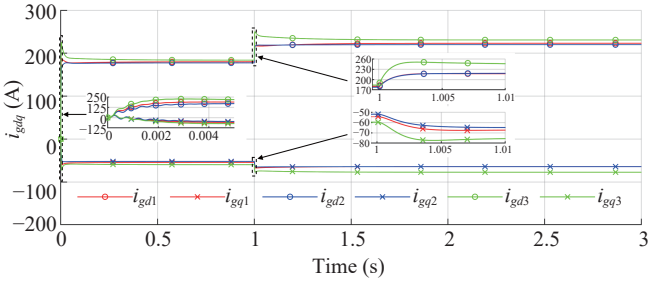

Fig. 23. Injected grid currents from DGs for Case 3.

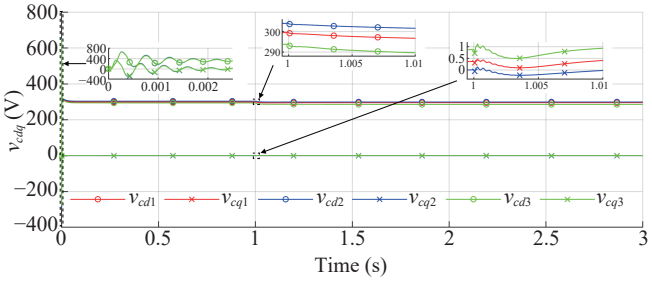

Fig. 24. Output capacitor voltages from DGs for Case 3.

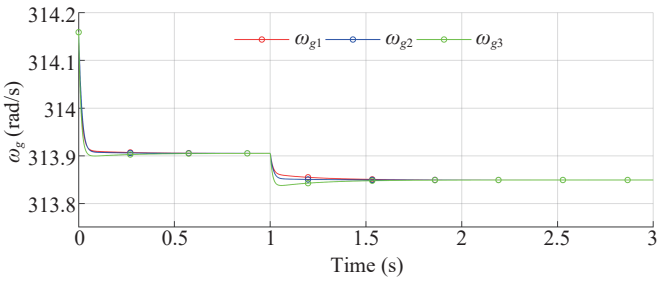

Fig. 25. Droop-governed VSC frequency from DGs for Case 3.

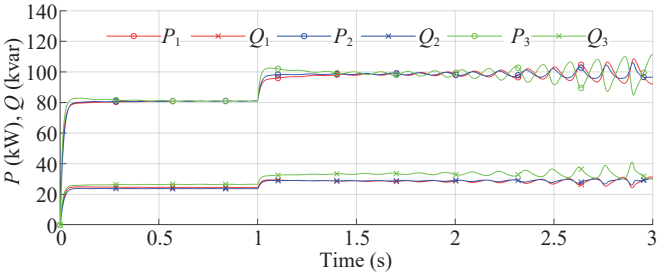

Fig. 26. Active and reactive power outputs from DGs for Case 4.

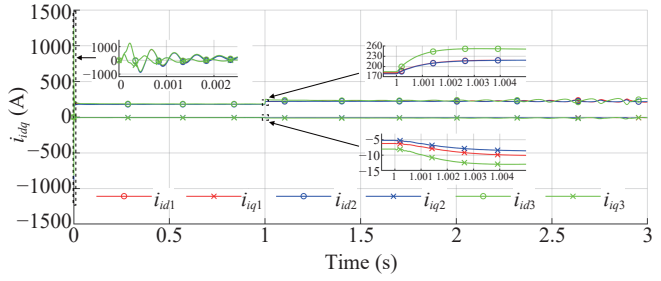

Fig. 27. Output VSC currents from DGs for Case 4.

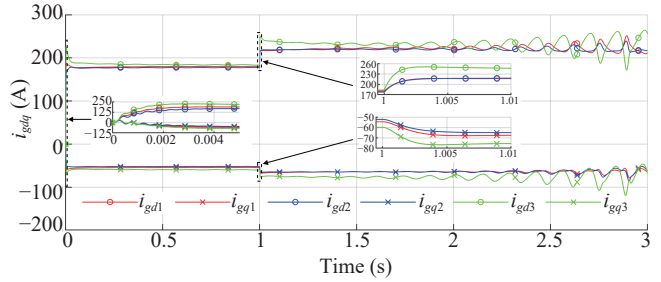

Fig. 28. Injected grid currents from DGs for Case 4.

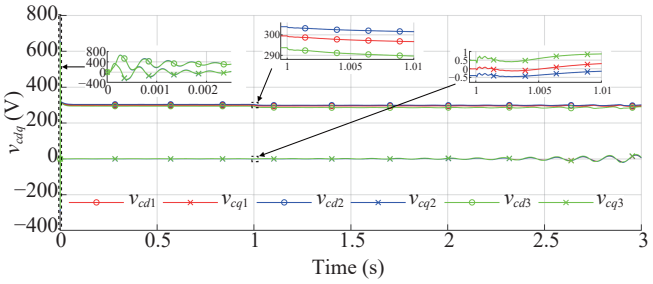

Fig. 29. Output capacitor voltages from DGs for Case 4.

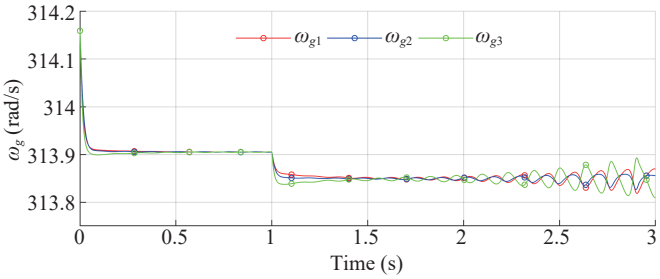

Fig. 30. Droop-governed VSC frequency from DGs for Case 4.

considered a more critical parameter in avoiding instability. The optimization framework developed aids in mitigating this effect on stability from the boost converter subsystem and leads to a desirable dynamic performance. It would be interesting to investigate the relations between R_{onb} and R_{lb} with regards to obtaining necessary and sufficient conditions for preserving stability in the boost converter subsystem of VSC-MGs.

4) Impact on Different Operating Conditions

The optimized boost converter parameters obtained, $R_{lb} = 0.001\ \Omega$, $L_{lb} = 800\ \mu$H, and $R_{onb} = 2.16548\ \Omega$, are analyzed in different operating conditions described in subsection III-C and mode locations associated with the boost converter subsystem in these conditions are shown in Table IX. The table is consistent with Case 3 in Table VII showing that modes m_{18}^{17}–m_{22}^{21} remain largely sensitive to states of the VSC's power controller with some influence from states of the boost converter's power model, whereas modes m_{24}^{23}–m_{28}^{27} in the high frequency range that are largely sensitive to states of the boost converter's power model are moved further to the left of the complex plane. Results in Table IX reconfirm that small-signal stability is almost independent of the operating condition, and hence the optimized boost converter parameters using one operation condition is sufficient for other operating conditions in the VSC-MG.

TABLE IX
BOOST CONVERTER ASSOCIATED MODE LOCATIONS USING OPTIMIZED PARAMETERS AT DIFFERENT OPERATING CONDITIONS

$m_{\#}$	OC 1	OC 2	OC 3	OC 4	OC 5	OC 6
m_{18}^{17}	−99.90 ±j132.20	−117.49 ±j135.08	−107.47 ±j133.89	−116.54 ±j134.47	−113.02 ±j134.63	−121.27 ±j135.31
m_{20}^{19}	−104.58 ±j133.09	−121.52 ±j135.21	−122.38 ±j135.22	−122.99 ±j134.62	−117.35 ±j135.00	−131.55 ±j138.66
m_{22}^{21}	−104.84 ±j133.81	−121.81 ±j135.73	−116.52 ±j135.40	−116.74 ±j134.92	−117.46 ±j135.55	−130.97 ±j139.62
m_{24}^{23}	−4659.2 ±j9330.3	−4187.4 ±j12067	−4643.6 ±j10146	−4415.0 ±j11366	−4406.0 ±j11398	−3943.1 ±j12663
m_{26}^{25}	−4664.3 ±j9451.0	−4158.9 ±j12132	−4376.8 ±j11502	−4395.4 ±j11441	−4402.7 ±j11409	−3927.1 ±j12699
m_{28}^{27}	−4666.8 ±j9465.6	−4165.2 ±j12134	−4061.4 ±j12390	−4397.8 ±j11425	−4397.0 ±j11435	−3922.3 ±j12704

V. CONCLUSION

Small-signal stability analysis is applied in this paper to investigate the behavior of a PI-based controller used in the boost converter subsystem and an IMC-based controller used in the VSC subsystem. Both subsystems are parts of a DER supplying power to loads in an islanded VSC-MG network. The effects of the digital controller's time delay for both subsystems and an LCL filter accounting for the VSC's dead-time is incorporated in the complete state-space model of the VSC-MG. The analysis reveals boost converter parameters R_{lb}, L_{lb}, and R_{onb} are critical as they contribute towards shaping the trajectories of the dominant modes in the VSC-MG network. It can be concluded that these parameters have varying effects on stability and therefore cannot be disregarded even in the presence of the VSC's power controller impacting other low frequency dominant modes. Analysis within the domain of stability for these boost converter parameters reveals that cases could exist where instability in the boost converter subsystem is propagated to the VSC subsystem. The optimization framework developed utilizing particle swarm optimization considers dynamic coupling between both subsystems while addressing aspects of small-signal stability by avoiding inadequate parameters in designing the VSC-MG. Resulting optimized boost converter parameters obtained demonstrated better transient behavior and illustrated that by carefully selecting these parameters, effects on instability from the boost converter subsystem can be mitigated.

REFERENCES

[1] S. K. Sahoo, A. K. Sinha, and N. K. Kishore, "Control techniques in AC, DC, and hybrid AC–DC microgrid: A review," *IEEE Journal of Emerging and Selected Topics in Power Electronics*, vol. 6, no. 2, pp. 738–759, Jun. 2018.

[2] S. Parhizi, H. Lotfi, A. Khodaei, and S. Bahramirad, "State of the art in research on microgrids: A review," *IEEE Access*, vol. 3, pp. 890–925, Jun. 2015.

[3] M. Farrokhabadi, C. A. Canizares, J. W. Simpson-Porco, E. Nasr, L. L. Fan, P. A. Mendoza-Araya, R. Tonkoski, U. Tamrakar, N. Hatziargyriou, D. Lagos, R. W. Wies, M. Paolone, M. Liserre, L. Meegahapola, M. Kabalan, A. H. Hajimiragha, D. Peralta, M. A. Elizondo, K. P. Schneider, F. K. Tuffner, and J. Reilly, "Microgrid stability definitions, analysis, and examples," *IEEE Transactions on Power Systems*, vol. 35, no. 1, pp. 13–29, Jan. 2020.

[4] A. S. Vijay, D. K. Dheer, A. Tiwari, and S. Doolla, "Performance evaluation of homogeneous and heterogeneous droop-based systems in microgrid—stability and transient response perspective," *IEEE Transactions on Energy Conversion*, vol. 34, no. 1, pp. 36–46, Mar. 2019.

[5] M. Yazdanian and A. Mehrizi-Sani, "Case studies on cascade voltage control of islanded microgrids based on the internal model control," *IFAC-PapersOnLine*, vol. 48, no. 30, pp. 578–582, Dec. 2015.

[6] C. E. Garcia and M. Morari, "Internal model control. A unifying review and some new results," *Industrial & Engineering Chemistry Process Design and Development*, vol. 21, no. 2, pp. 308–323, Apr. 1982.

[7] B. A. Francis and W. M. Wonham, "The internal model principle of control theory," *Automatica*, vol. 12, no. 5, pp. 457–465, Sep. 1976.

[8] D. E. Rivera, M. Morari, and S. Skogestad, "Internal model control: PID controller design," *Industrial & Engineering Chemistry Process Design and Development*, vol. 25, no. 1, pp. 252–265, Jan. 1986.

[9] S. Leitner, M. Yazdanian, A. Mehrizi-Sani, and A. Muetze, "Small-signal stability analysis of an inverter-based microgrid with internal model-based controllers," *IEEE Transactions on Smart Grid*, vol. 9, no. 5, pp. 5393–5402, Sep. 2018.
[10] N. Pogaku, M. Prodanovic, and T. C. Green, "Modeling, analysis and testing of autonomous operation of an inverter-based microgrid," *IEEE Transactions on Power Electronics*, vol. 22, no. 2, pp. 613–625, Mar. 2007.
[11] W. H. Li and X. N. He, "Review of nonisolated high-step-up DC/DC converters in photovoltaic grid-connected applications," *IEEE Transactions on Industrial Electronics*, vol. 58, no. 4, pp. 1239–1250, Apr. 2011.
[12] Y. B. Wang, X. F. Wang, F. Blaabjerg, and Z. Chen, "Harmonic instability assessment using state-space modeling and participation analysis in inverter-fed power systems," *IEEE Transactions on Industrial Electronics*, vol. 64, no. 1, pp. 806–816, Jan. 2017.
[13] A. Rodríguez-Cabero, M. Prodanovic, and J. Roldán-Perez, "Analysis of dynamic properties of VSCs connected to weak grids including the effects of dead time and time delays," *IEEE Transactions on Sustainable Energy*, vol. 10, no. 3, pp. 1066–1075, Jul. 2019.
[14] B. Banković, F. Filipoviić, N. Mitroviić, M. Petronijeviić, and V. Kostiić, "A building block method for modeling and small-signal stability analysis of the autonomous microgrid operation," *Energies*, vol. 13, no. 6, pp. 1492, Mar. 2020.
[15] J. Sun, "Two-port characterization and transfer immittances of AC–DC converters–part II: Applications," *IEEE Open Journal of Power Electronics*, vol. 2, pp. 483–510, Aug. 2021.
[16] L. Herrera, E. Inoa, F. Guo, J. Wang, and H. N. Tang, "Small-signal modeling and networked control of a PHEV charging facility," *IEEE Transactions on Industry Applications*, vol. 50, no. 2, pp. 1121–1130, Mar./Apr./ 2014.
[17] D. Dong, I. Cvetkovic, D. Boroyevich, W. Zhang, R. Wang, and P. Mattavelli, "Grid-interface bidirectional converter for residential DC distribution systems—part one: High-density two-stage topology," *IEEE Transactions on Power Electronics*, vol. 28, no. 4, pp. 1655–1666, Apr. 2013.
[18] H. Mejbri, K. Ammous, H. Morel, and A. Ammous, "Multi-objective optimization of power converter sizing based on genetic algorithms: Application to photovoltaic systems," *International Review on Modelling and Simulations*, vol. 5, no. 2, pp. 826–839, Apr. 2012.
[19] M. Mirjafari, S. Harb, and R. S. Balog, "Multiobjective optimization and topology selection for a module-integrated inverter," *IEEE Transactions on Power Electronics*, vol. 30, no. 8, pp. 4219–4231, Aug. 2015.
[20] J. L. Agorreta, M. Borrega, J. López, and L. Marroyo, "Modeling and control of *N*-paralleled grid-connected inverters with LCL filter coupled due to grid impedance in PV plants," *IEEE Transactions on Power Electronics*, vol. 26, no. 3, pp. 770–785, Mar. 2011.
[21] W. S. Levine, *Control System Fundamentals*, 2nd ed., Boca Raton, Florida: CRC Press, 2011.
[22] S. Ahmed, Z. Y. Shen, P. Mattavelli, D. Boroyevich, and K. J. Karimi, "Small-signal model of voltage source inverter (VSI) and voltage source converter (VSC) considering the deadtime effect and space vector modulation types," *IEEE Transactions on Power Electronics*, vol. 32, no. 6, pp. 4145–4156, Jun. 2017.
[23] A. Rodríguez-Cabero, J. Roldán-Pérez, and M. Prodanovic, "Virtual impedance design considerations for virtual synchronous machines in weak grids," *IEEE Journal of Emerging and Selected Topics in Power Electronics*, vol. 8, no. 2, pp. 1477–1489, Jun. 2020.
[24] A. Yazdani and R. Iravani, *Voltage-Sourced Converters in Power Systems: Modeling, Control, and Applications*, Hoboken, New Jersey: John Wiley & Sons, 2010.
[25] E. Barklund, N. Pogaku, M. Prodanovic, C. Hernandez-Aramburo, and T. C. Green, "Energy management in autonomous microgrid using stability-constrained droop control of inverters," *IEEE Transactions on Power Electronics*, vol. 23, no. 5, pp. 2346–2352, Sep. 2008.
[26] Z. X. Miao, A. Domijan, and L. L. Fan, "Investigation of microgrids with both inverter interfaced and direct AC-connected distributed energy resources," *IEEE Transactions on Power Delivery*, vol. 26, no. 3, pp. 1634–1642, Jul. 2011.
[27] A. Aderibole, H. H. Zeineldin, M. S. El-Moursi, J. C. H. Peng, and M. Al Hosani, "Domain of stability characterization for hybrid microgrids considering different power sharing conditions," *IEEE Transactions on Energy Conversion*, vol. 33, no. 1, pp. 312–323, Mar. 2018.
[28] J. Kennedy and R. Eberhart, "Particle swarm optimization," in *Proceedings of the International Conference on Neural Networks*, 1995, pp. 1942–1948.
[29] Y. del Valle, G. K. Venayagamoorthy, S. Mohagheghi, J. C. Hernandez, and R. G. Harley, "Particle swarm optimization: Basic concepts, variants and applications in power systems," *IEEE Transactions on Evolutionary Computation*, vol. 12, no. 2, pp. 171–195, Apr. 2008.

Chiebuka Eyisi received the B.Sc. degree in Electrical/Electronic Engineering from Kwame Nkrumah University of Science and Technology, Kumasi, Ghana, in 2010 and the M.Sc. degree in Electrical Engineering from the University of Central Florida, Orlando, FL, USA, in 2013. His research interests include power system optimization, renewable energy integration, and stability analysis of microgrids.

Qifeng Li received the Ph.D. degree in Electrical Engineering from Arizona State University, Tempe, AZ, in 2016. He is currently an Assistant Professor with the Department of Electrical and Computer Engineering, the University of Central Florida (UCF), Orlando, FL, USA. Before joining UCF Faculty, he held a position of Postdoctoral Associate with the Department of Mechanical Engineering, Massachusetts Institute of Technology (MIT), Cambridge, MA, USA, from 2016 to 2018. His research interests include convex optimization, uncertainty-aware optimization, and nonlinear systems with applications in power and energy systems